Monthly Notices
of the
ROYAL ASTRONOMICAL SOCIETY

MNRAS **474,** 1116–1134 (2018)
Advance Access publication 2017 November 1

doi:10.1093/mnras/stx2837

KiDS-450: cosmological constraints from weak lensing peak statistics – I. Inference from analytical prediction of high signal-to-noise ratio convergence peaks

HuanYuan Shan,[1★] Xiangkun Liu,[2,3★] Hendrik Hildebrandt,[1] Chuzhong Pan,[3] Nicolas Martinet,[1] Zuhui Fan,[3] Peter Schneider,[1] Marika Asgari,[4] Joachim Harnois-Déraps,[4] Henk Hoekstra,[5] Angus Wright,[1] Jörg P. Dietrich,[6,7] Thomas Erben,[1] Fedor Getman,[8] Aniello Grado,[8] Catherine Heymans,[4] Dominik Klaes,[1] Konrad Kuijken,[9] Julian Merten,[10,11] Emanuella Puddu,[8] Mario Radovich[12] and Qiao Wang[13]

[1]*Argelander-Institut für Astronomie, Auf dem Hügel 71, D-53121 Bonn, Germany*
[2]*South-Western Institute for Astronomy Research, Yunnan University, Kunming 650500, China*
[3]*Department of Astronomy, School of Physics, Peking University, Beijing 100871, China*
[4]*Institute for Astronomy, University of Edinburgh, Royal Observatory, Blackford Hill, Edinburgh EH9 3HJ, UK*
[5]*Leiden Observatory, Leiden University, PO Box 9513, NL-2300 RA Leiden, the Netherlands*
[6]*Faculty of Physics, Ludwig-Maximilians-Universität, Scheinerstr. 1, D-81679 Munich, Germany*
[7]*Excellence Cluster Universe, Boltzmannstr. 2, D-85748 Garching, Germany*
[8]*INAF – Astronomical Observatory of Capodimonte, Via Moiariello 16, I-80131 Napoli, Italy*
[9]*Leiden University, PO Box 9513, NL-2300 RA Leiden, the Netherlands*
[10]*Department of Physics, University of Oxford, Keble Road, Oxford OX1 3RH, UK*
[11]*INAF, Osservatorio Astronomico di Bologna, via Pietro Gobetti 93/3, I-40129 Bologna, Italy*
[12]*INAF – Osservatorio Astronomico di Padova, via dell'Osservatorio 5, I-35122 Padova, Italy*
[13]*Key laboratory for Computational Astrophysics, National Astronomical Observatories, Chinese Academy of Sciences, Beijing 100012, China*

Accepted 2017 October 30. Received 2017 October 30; in original form 2017 September 22

ABSTRACT

This paper is the first of a series of papers constraining cosmological parameters with weak lensing peak statistics using ∼450 deg^2 of imaging data from the Kilo Degree Survey (KiDS-450). We measure high signal-to-noise ratio (SNR: ν) weak lensing convergence peaks in the range of $3 < \nu < 5$, and employ theoretical models to derive expected values. These models are validated using a suite of simulations. We take into account two major systematic effects, the boost factor and the effect of baryons on the mass–concentration relation of dark matter haloes. In addition, we investigate the impacts of other potential astrophysical systematics including the projection effects of large-scale structures, intrinsic galaxy alignments, as well as residual measurement uncertainties in the shear and redshift calibration. Assuming a flat Λ cold dark matter model, we find constraints for $S_8 = \sigma_8(\Omega_m/0.3)^{0.5} = 0.746^{+0.046}_{-0.107}$ according to the degeneracy direction of the cosmic shear analysis and $\Sigma_8 = \sigma_8(\Omega_m/0.3)^{0.38} = 0.696^{+0.048}_{-0.050}$ based on the derived degeneracy direction of our high-SNR peak statistics. The difference between the power index of S_8 and in Σ_8 indicates that combining cosmic shear with peak statistics has the potential to break the degeneracy in σ_8 and Ω_m. Our results are consistent with the cosmic shear tomographic correlation analysis of the same data set and $\sim 2\sigma$ lower than the *Planck* 2016 results.

Key words: gravitational lensing: weak – dark matter – large-scale structure of Universe.

★ E-mail: shanhuany@gmail.com (HYS); liuxk@ynu.edu.cn (XL)

1 INTRODUCTION

Large-scale structures (LSS) in the Universe produce coherent distortions on the image of background galaxies, an effect caused by weak gravitational lensing (WL) and generally known as cosmic shear. By measuring the shapes of these galaxies, we are able to extract information about the foreground matter distribution (Bartelmann & Schneider 2001). This is an important cosmological probe; however, the shear signals are very weak, typically a few per cent. In order to be able to measure cosmological parameters, we need very accurate shape measurements for a vast number of distant faint and small galaxies, which is extremely challenging. Tremendous efforts have been made in observational developments (e.g. Erben et al. 2013; de Jong et al. 2015, 2017; Kuijken et al. 2015; Hildebrandt et al. 2016; Jarvis et al. 2016; Aihara et al. 2017; Mandelbaum et al. 2017; Zuntz et al. 2017), and methodological advances in extracting shape information (e.g. Hoekstra et al. 2015; Mandelbaum et al. 2015; Fenech Conti et al. 2017) and in statistical analysis (see Kilbinger 2015, and references therein). These have proved the feasibility of using WL effects in cosmological studies. The results from recent large surveys, including the Canada–France–Hawaii Telescope Lensing Survey (CFHTLenS;[1] Heymans et al. 2012), the Kilo Degree Survey (KiDS;[2] Hildebrandt et al. 2017) and the Dark Energy Survey (DES;[3] Troxel et al. 2017), have further strengthened their important roles. With ongoing and next-generation surveys, such as the Subaru Hyper Suprime-Cam[4] lensing survey (Aihara et al. 2017), *Euclid*[5] (Laureijs et al. 2011), the Large Synoptic Survey Telescope (LSST;[6] Abell et al. 2009), WL will become one of the main cosmological probes, realizing that much tighter controls of systematics are necessary.

The recent cosmic shear two-point correlation function (2PCF) analysis using data from 450 square degrees of the Kilo Degree Survey (in Hildebrandt et al. 2017, KiDS-450 hereafter) found a 2.3σ tension on the value of $S_8 = \sigma_8(\Omega_m/0.3)^{0.5}$ in comparison with that expected from the cosmic microwave background (CMB) measurements of the *Planck* satellite (Planck Collaboration XIII 2016a). Here Ω_m and σ_8 are, respectively, the present matter density in units of the critical density and the root mean square (rms) of the linear density fluctuations smoothed on a scale of $8\,h^{-1}$ Mpc. The KiDS-450 constraints are in agreement with other cosmic shear studies (Heymans et al. 2013; Joudaki et al. 2017a; Troxel et al. 2017), galaxy–galaxy lensing (Leauthaud et al. 2017) and pre-*Planck* CMB constraints (Calabrese et al. 2017). Understanding such a tension is currently an important aspect of research in the field.

The typical mean redshift of source galaxies in current WL surveys is $z < 1$, and thus the WL signal is sensitive to late-time structure formation. On the other hand, the CMB properties are primarily affected by physical processes at early times. The tension between the results obtained from these two probes might indicate missing ingredients in our current cosmological model. To answer this, however, we need to first scrutinize carefully whether the tension arises unphysically from residual systematic errors in the analysis of different probes. For WL probes, different statistical quantities can respond differently to systematics. Thus, it is helpful to perform cosmological studies with same WL data, but using different statistical analyses. In this paper, we perform a WL peak analysis using the KiDS-450 data, derive an independent measurement of S_8 and compare our results with the cosmic shear results obtained from Hildebrandt et al. (2017).

In WL cosmological studies, the cosmic shear two-point statistics are the most commonly used statistical tools in probing the nature of dark matter (DM) and the origin of the current accelerating expansion of the Universe (e.g. Heymans et al. 2013; Kilbinger et al. 2013; Jarvis et al. 2016; Jee et al. 2016; Hildebrandt et al. 2017; Joudaki et al. 2017a; Troxel et al. 2017). It is, however, insensitive to the non-Gaussian information encoded in non-linear structure formation. WL peaks, on the other hand, are high-signal regions, which are closely associated with massive structures along the line of sight (LOS). Their statistics is a simple and effective way to capture the non-Gaussian information in the WL field, and thus highly complementary to the cosmic shear 2PCF (e.g. Kruse & Schneider 1999; Dietrich & Hartlap 2010; Marian et al. 2012, 2013; Shan et al. 2012, 2014; Hamana et al. 2015; Lin & Kilbinger 2015; Liu et al. 2015a, Liu et al. 2015b, 2016; Martinet et al. 2015; Kacprzak et al. 2016).

With recent wide-field WL imaging surveys, several measurements of WL peak counts have been performed, and subsequent cosmological constraints have been derived. With the shear catalogue (Miller et al. 2013) from CFHTLenS, Liu et al. (2015a) generated convergence maps with various Gaussian smoothing scales, and identified peaks from the maps as local maxima. Based on interpolations from a set of simulation templates with varying cosmological parameters (Ω_m, σ_8, w), constraints on these were obtained. Combining WL peak counts with the convergence power spectrum, they found that the constraints can be improved by a factor of about 2. Considering the high-SNR (signal-to-noise ratio) peaks in the Canada–France–Hawaii Telescope Stripe 82 survey (CS82), Liu et al. (2015b) derived constraints on cosmological parameters (Ω_m, σ_8) using the theoretical model of Fan, Shan & Liu (2010). With the same method, Liu et al. (2016b) presented constraints on the $f(R)$ theory with the CFHTLenS data. Kacprzak et al. (2016) measured the shear peaks using aperture mass maps (Schneider 1996; Bartelmann & Schneider 2001) from the Dark Energy Survey Science Verification (DES-SV) data. To derive cosmological constraints, they also adopted the simulation approach to produce WL maps (Dietrich & Hartlap 2010) spanning the (Ω_m, σ_8) plane.

Compared to cosmological studies with clusters of galaxies (Vikhlinin et al. 2009; Rozo et al. 2010; Planck Collaboration XXIV 2016b), WL peak statistics can provide cosmological constraints that are free from potential selection effects (Angulo et al. 2012) and biases associated with cluster mass estimates.

The correspondence between WL peaks and DM haloes is not one to one. Indeed, most of the low-SNR peaks are usually not associated with a dominant halo, and are instead generated by the projection of LSS along the LOS. Even for high-SNR peaks where the correspondence with massive haloes is clearly seen, many systematic effects, such as the shape noise contamination from the intrinsic ellipticities of source galaxies, the boost factor due to the member contamination and the blending in cluster regions, baryonic effects, the projection effects of LSS and intrinsic alignments (IA), can complicate WL peak analysis (Tang & Fan 2005; Yang et al. 2011, 2013; Hamana et al. 2012; Fu & Fan 2014; Osato, Shirasaki & Yoshida 2015; Kacprzak et al. 2016; Liu & Haiman 2016; Yuan et al. 2017). These can generate non-halo-associated peaks and also alter the significance of the peaks from

[1] http://www.cfhtlens.org/
[2] http://kids.strw.leidenuniv.nl/
[3] http://www.darkenergysurvey.org/
[4] http://hsc.mtk.nao.ac.jp/ssp/
[5] http://sci.esa.int/euclid/
[6] http://www.lsst.org/

DM haloes, thus affecting WL peak statistics. Understanding and quantifying these effects is key to connect the observed peak signal to the underlying cosmology.

There are different approaches to predict WL peak counts: (i) generating WL simulation templates densely sampled in cosmological parameter space (Dietrich & Hartlap 2010; Liu et al. 2015a; Kacprzak et al. 2016); (ii) theoretical modelling taking into account different systematic effects, using either a pure Gaussian random field analysis (Maturi et al. 2010) or a halo model plus the Gaussian random noise applicable to high-SNR peaks (Fan et al. 2010; Yuan et al. 2017); (iii) modelling a stochastic process to predict WL peak counts by producing lensing maps using a halo distribution from a theoretical halo mass function (Lin & Kilbinger 2015). This is physically similar to the halo model.

In this work, we perform WL peak studies using the KiDS-450 data. To confront the tension on S_8 measurement, we derive an independent constraint on S_8 from the abundance of high-SNR peaks adopting the analytical model of Fan et al. (2010), in which the dominant shape noise effects have been fully taken into account. We further explore the potential systematics on WL peak statistics. We compare our results with the ones derived from the tomographic cosmic shear measurement from Hildebrandt et al. (2017), as well as those from previous WL peak studies. We also observe a difference between the degeneracy direction of $(\Omega_{\rm m}, \sigma_8)$ in WL peak statistics and in cosmic shear analysis. Therefore, instead of S_8, we use $\Sigma_8 = \sigma_8(\Omega_{\rm m}/0.3)^{\alpha}$ and fit the slope α to the data.

This is the first of a series of papers on cosmological constraints from WL peak statistics using KiDS-450. In the subsequent paper, by comparing with simulation templates from Dietrich & Hartlap (2010), Martinet et al. (2017) derive constraints with shear peak statistics identified from aperture mass maps. Because the projection effects of LSS are included in the simulations, an independent measurement of the value of S_8 can be obtained with the low- and medium-SNR peaks. The different physical origins of low- and high-SNR peaks indicate different cosmological information embedded in the peak statistics of different ranges. Furthermore, we expect that the systematics affect these two analyses in different ways. Therefore, the consistency between the results from the two studies indicates their robustness.

This paper is structured as follows: in Section 2, we describe the KiDS-450 data set. In Section 3, we present the procedures of WL peak analysis. In Section 4, we discuss the systematic effects. In Section 5, we derive the cosmological constraints with WL peak counts. A summary and discussion are given in Section 6.

2 THE KIDS-450 DATA

The ongoing KiDS (de Jong et al. 2015; Kuijken et al. 2015), designed for WL studies, is a 1350 deg^2 optical imaging survey in four bands (u, g, r, i) with 5σ limiting magnitudes of 24.3, 25.1, 24.9, 23.8, respectively, using the OmegaCAM CCD camera mounted at the Cassegrain focus of the VLT Survey Telescope.

In this paper, we use the KiDS-450 shear catalogue (de Jong et al. 2017; Hildebrandt et al. 2017), which consists of 454 tiles covering a total area of 449.7 deg^2. After excluding the masked regions, the effective survey area is 360.3 deg^2. The lensing measurements are performed on the r-band images with median seeing 0.66 arcsec. The KiDS-450 r-band images are processed with the THELI pipeline, which has been optimized for lensing applications (Erben et al. 2009, 2013). As the observing strategy of the KiDS survey was motivated to cover the Galaxy And Mass Assembly (GAMA) fields (Liske et al. 2015), the KiDS-450 data set contains five patches (G9, G12, G15, G23, GS), covering (45.95, 91.96, 89.60, 81.61, 51.16) deg^2, respectively.

Photometric redshifts (photo-z) $z_{\rm B}$ are derived using the Bayesian point estimates from BPZ (Benitez 2000; Hildebrandt et al. 2012). The source redshift distribution $n(z)$ is calculated through a weighted direct calibration technique based on the overlap with deep spectroscopic surveys (the so-called DIR method; Hildebrandt et al. 2017).

The ellipticities of the galaxies are derived using a 'self-calibrating' version of the shape measurement method LENSFIT (Miller et al. 2013; Fenech Conti et al. 2017). The multiplicative shear calibration bias, m, is obtained from image simulations with $\sim$1 per cent error for galaxies with $z_{\rm B} \leq 0.9$. The additive shear calibration bias c is estimated empirically from the data by averaging galaxy ellipticities in the different patches and redshift bins.

In this paper, we first split the galaxy sample into four tomographic bins $z_{\rm B} = ([0.1, 0.3], [0.3, 0.5], [0.5, 0.7], [0.7, 0.9])$ per patch as in Hildebrandt et al. (2017), and apply shear calibration corrections per tomographic bin and patch. The additive correction is done on individual galaxies, and the multiplicative correction is performed statistically (see equation 8). Because of the low effective number density $n_{\rm eff} \sim 7.5$ galaxies arcmin^{-2} within $0.1 < z_{\rm B} \leq 0.9$ of KiDS-450, there are only $\sim$2 galaxies arcmin^{-2} in each redshift bin. Such low number densities prevent us from performing WL peak analysis tomographically at this stage. Therefore, after the correction, we then combine all the galaxies with $0.1 < z_{\rm B} \leq 0.9$ for WL peak count analysis.

3 WEAK LENSING PEAK ANALYSIS

3.1 Theoretical basics

The distortion of galaxy shapes by the gravitational lensing effect can be described by the Jacobian matrix $\mathbf{A}$, which is given by (e.g. Bartelmann & Schneider 2001)

$$\mathbf{A} = (1-\kappa)\begin{pmatrix} 1-g_1 & -g_2 \\ -g_2 & 1+g_1 \end{pmatrix}, \quad (1)$$

where $\boldsymbol{g} = \frac{\boldsymbol{\gamma}}{1-\kappa}$ is the reduced shear written in the complex form of $g_1 + {\rm i}g_2$. The quantities $\boldsymbol{\gamma}$ and κ are the complex lensing shear and convergence, respectively. They can be calculated from the second derivatives of the lensing potential, and thus $\boldsymbol{\gamma}$ and κ are not independent quantities. The convergence κ is related to the projected matter density along the LOS scaled by a geometric factor.

The observed lensing quantity is the complex ellipticity $\boldsymbol{\epsilon}$, which contains both the reduced shear and shape noise from the intrinsic galaxy ellipticity (Seitz & Schneider 1997). In order to identify WL peaks, we need to relate the shear to the convergence, which involves a mass reconstruction algorithm. To reduce the noise from finite measurements of the shear, the observed ellipticities are regularized on a mesh and smoothed by a filter function. This results in an estimate of the smoothed field of the reduced shear $\boldsymbol{g}$. From that, the convergence field can be reconstructed with the non-linear Kaiser–Squires (KS) inversion (Kaiser & Squires 1993; Kaiser, Squires & Broadhurst 1995; Seitz & Schneider 1995). We can then identify WL peaks, defined as local maxima in the two-dimensional convergence field. Their abundance contains important cosmological information that we analyse in this paper.

In our analysis, we construct the convergence map tile by tile. Each KiDS tile is 1 deg^2. In order to keep more effective area while excluding the problematic boundary, we extend each tile to 1.2×1.2 deg^2 using data from neighbouring tiles. The regular mesh

in each convergence map contains 512 × 512 pixels with a pixel size of ∼0.14 arcmin. Then, the outermost 43 pixels (∼6 arcmin) along each side of the extended tile boundaries are excluded to suppress the boundary effects. Moreover, for area of this size, we expect an insignificant mass-sheet degeneracy contribution (Falco, Gorenstein & Shapiro 1985).

As described above, we smooth the pixelated ellipticity field with a Gaussian function,

$$W_{\theta_{\rm G}}(\boldsymbol{\theta}) = \frac{1}{\pi\theta_{\rm G}^2}\exp\left(-\frac{|\boldsymbol{\theta}|^2}{\theta_{\rm G}^2}\right), \tag{2}$$

where $\theta_{\rm G}$ is the smoothing scale. Hamana, Takada & Yoshida (2004) found that $\theta_{\rm G} \sim 1-2$ arcmin is an optimal choice for detecting massive haloes with $M \gtrsim 10^{14}\,h^{-1}\,{\rm M}_\odot$ at intermediate redshifts. In this paper, we take $\theta_{\rm G} = 2$ arcmin so that >30 galaxies can be included in the smoothing kernel effectively. Consequently, the Gaussian approximation for the shape noise field should be valid, according to the central limit theorem (Van Waerbeke 2000). The mean rms of the smoothed shape noise field is $\sigma_0 \sim 0.023$, much larger than the contribution from the projection effect of LSS (discussed in Section 4.3), hence is dominant on our smoothed convergence maps.

3.2 Weak lensing peak model

In this work, we adopt a theoretical approach to derive the cosmological constraints from WL peak counts. Fan et al. (2010) presented a model taking into account the effects of shape noise, including the noise-induced bias and dispersion on the SNR of true peaks corresponding to massive DM haloes, the spurious peaks induced by the shape noise of background sources, along with the enhancement of the pure noise peaks near massive DM haloes.

Specifically, this model assumes that the true high-SNR peaks are caused mainly by the existence of individual massive DM haloes (Hamana et al. 2004; Yang et al. 2011; Liu & Haiman 2016) and that the residual shape noise field is approximately Gaussian. Accordingly, the smoothed convergence field can be written as $\kappa_{\rm n}^{\rm (S)} = \kappa^{\rm (S)} + n^{\rm (S)}$, where $\kappa^{\rm (S)}$ represents the true lensing convergence from individual massive haloes and $n^{\rm (S)}$ is the residual Gaussian shape noise. Assuming that $\kappa^{\rm (S)}$ is known from the halo density profile, the field $\kappa_{\rm n}^{\rm (S)}$ is therefore a Gaussian random field modulated by $\kappa^{\rm (S)}$. The peak count distribution can therefore be derived using Gaussian statistics, in which the dependence on $\kappa^{\rm (S)}$ and its first and second derivatives $\kappa_i^{\rm (S)} = \partial\kappa^{\rm (S)}/\partial x_i$ and $\kappa_{ij}^{\rm (S)} = \partial^2\kappa^{\rm (S)}/\partial x_i\partial x_j (i = 1, 2)$ of $\kappa^{\rm (S)}$ reflect the modulation effect of DM haloes. The surface number density of convergence peaks can then be written as

$$n_{\rm peak}(\nu)d\nu = n_{\rm peak}^{\rm h}(\nu){\rm d}\nu + n_{\rm peak}^{\rm f}(\nu){\rm d}\nu, \tag{3}$$

where $\nu = \kappa/\sigma_0$ is the SNR of a peak, and $n_{\rm peak}^{\rm h}(\nu)$ and $n_{\rm peak}^{\rm f}$ denote the number densities of WL peaks within halo regions (the virial radius) and those in the field regions outside, respectively.

3.2.1 *Peaks in halo regions*

The peak count within halo regions, containing both the true peaks from the DM haloes and noise peaks therein, can be written as

$$n_{\rm peak}^{\rm h}(\nu) = \int {\rm d}z \frac{{\rm d}V(z)}{{\rm d}z\,{\rm d}\Omega}\int_{M_{\rm lim}} {\rm d}M\, n(M, z)\, f_{\rm p}(\nu, M, z), \tag{4}$$

where ${\rm d}V(z)$ is the cosmological volume element at redshift z, ${\rm d}\Omega$ is the solid angle element and $n(M, z)$ is the halo mass function, for which we adopt the function obtained by Watson et al. (2013). Note that the model concerns high-SNR peaks, which are mainly due to a single massive halo. We thus apply a lower mass limit $M_{\rm lim}$, and only haloes with mass $M > M_{\rm lim}$ contribute to the integration in equation (4). From our investigation with mock data (Appendix C), we find that (1) a mass limit $M_{\rm lim} = 10^{14}\,h^{-1}\,{\rm M}_\odot$ for peaks with $\nu > 3$ is a suitable choice that is also physically meaningful, as it corresponds to clusters of galaxies; (2) the input cosmological parameters can be well recovered, suggesting that the impact of the uncertainties in the model ingredients, such as the halo mass function, is insignificant concerning the current study. The term $f_{\rm p}$ denotes the number of peaks within the virial radius of a DM halo, and is given by

$$f_{\rm p}(\nu, M, z) = \int_0^{\theta_{\rm vir}} {\rm d}\theta\, (2\pi\theta)\, \hat{n}_{\rm peak}^{\rm c}(\nu, \theta, M, z), \tag{5}$$

where $\theta_{\rm vir} = R_{\rm vir}(M, z)/D_{\rm A}(z)$ is the angular virial radius, and $D_{\rm A}$ is the angular diameter distance to the DM halo. The physical virial radius $R_{\rm vir}$ is calculated by

$$R_{\rm vir}(M, z) = \left[\frac{3M}{4\pi\rho(z)\Delta_{\rm vir}(z)}\right]^{1/3}, \tag{6}$$

where $\rho(z)$ is the background matter density of the Universe at redshift z and the overdensity $\Delta_{\rm vir}$ is taken from Henry (2000). In our modelling, we limit the angular halo regions to $\theta_{\rm vir}$. The mass distributions outside it are regarded as parts of LSS contributions. Yuan et al. (2017) investigate in detail the LSS effects on peak statistics. For KiDS450, they are subdominant comparing to the impacts from shape noise.

The function $\hat{n}_{\rm peak}^{\rm c}(\nu, \theta, M, z)$ describes the surface number density of peaks at the location of θ from the centre of a halo, which can be derived using the theory of Gaussian random fields including the modulation effects from the DM halo contribution as follows:

$$\begin{aligned}\hat{n}_{\rm peak}^{\rm c}(\nu, \theta, M, z) = {} & \exp\left[-\frac{(\kappa_1^{\rm (S)})^2 + (\kappa_2^{\rm (S)})^2}{\sigma_1^2}\right] \\ & \times \left[\frac{1}{2\pi\theta_*^2}\frac{1}{(2\pi)^{1/2}}\right]\exp\left[-\frac{1}{2}\left(\nu - \frac{\kappa^{\rm (S)}}{\sigma_0}\right)^2\right] \\ & \times \int_0^\infty {\rm d}x_N \left\{\frac{1}{[2\pi(1-\gamma_N^2)]^{1/2}}\right. \\ & \times \exp\left[-\frac{[x_N + (\kappa_{11}^{\rm (S)} + \kappa_{22}^{\rm (S)})/\sigma_2 - \gamma_N(\nu_0 - \kappa^{\rm (S)}/\sigma_0)]^2}{2(1-\gamma_N^2)}\right] \\ & \left. \times F(x_N)\right\},\end{aligned} \tag{7}$$

with

$$\begin{aligned}F(x_N) = {} & \exp\left[-\frac{(\kappa_{11}^{\rm (S)} - \kappa_{22}^{\rm (S)})^2}{\sigma_2^2}\right] \\ & \times \int_0^{1/2} {\rm d}e_N\, 8(x_N^2 e_N)x_N^2(1-4e_N^2)\exp(-4x_N^2 e_N^2) \\ & \times \int_0^\pi \frac{{\rm d}\theta_N}{\pi}\, \exp\left[-4x_N e_N \cos(2\theta_N)\frac{(\kappa_{11}^{\rm (S)} - \kappa_{22}^{\rm (S)})}{\sigma_2}\right],\end{aligned} \tag{8}$$

where $\theta_*^2 = 2\sigma_1^2/\sigma_2^2$, $\gamma_N = \sigma_1^2/(\sigma_0\sigma_2)$. The quantities σ_i are the moments of the noise field $n^{(S)}$ given by (e.g. Van Waerbeke 2000)

$$\sigma_i^2 = \int \mathrm{d}k\, k^{2i} \langle |\widetilde{n}^{(S)}(k)|^2 \rangle, \tag{9}$$

where $\widetilde{n}^{(S)}(k)$ is the Fourier transform of the noise field $n^{(S)}$.

For the density profile of DM haloes, we adopt the Navarro–Frenk–White (NFW) distribution (Navarro, Frenk & White 1996, 1997):

$$\rho_{\rm NFW}(r) = \frac{\rho_{\rm s}}{(r/r_{\rm s})(1+r/r_{\rm s})^2}, \tag{10}$$

where $\rho_{\rm s}$ and $r_{\rm s}$ are the characteristic mass density and scale of a DM halo. The corresponding convergence κ is obtained by integrating to the infinity along the LOS. We then smooth with the Gaussian function $W_{\theta_{\rm G}}$ (equation 2) to calculate the halo terms $\kappa^{(S)}$, $\kappa_i^{(S)}$ and $\kappa_{ij}^{(S)}$.

We note that in WL analyses, there is not a consensus about the range of LOS integration for an NFW halo. We evaluate the impact of different LOS truncations on the peak analyses taking the models from Oguri & Hamana (2011). It is found that their effects on our considered peak numbers are all well within 1σ statistical fluctuations.

The mass–concentration relation given in Duffy et al. (2008) is adopted in the calculation. In our fiducial analyses, the amplitude of the mass–concentration relation is considered as a free parameter to be fitted by the data simultaneously with cosmological parameters.

For the redshift distribution of source galaxies, we take the DIR redshift distribution of KiDS-450 data in the fiducial analysis but also consider other cases to test for the effect of redshift uncertainties. The impact of the uncertainties in the source redshift distribution on the measured WL peak counts is estimated from 200 bootstrap resamples drawn from the full spectroscopic redshift training catalogue (Hildebrandt et al. 2017). By analysing different $n(z)$ distributions with the same pipeline, we find that our peak analysis is essentially unaffected within the redshift uncertainties. A similar conclusion is found in the cosmic shear analysis of Hildebrandt et al. (2017).

3.2.2 *Peaks in the field regions*

The density of pure noise peaks in the field region away from DM haloes is given by

$$n_{\rm peak}^{\rm f}(\nu) = \frac{1}{\mathrm{d}\Omega}\left\{ n_{\rm ran}(\nu)\left[\mathrm{d}\Omega - \int \mathrm{d}z \frac{\mathrm{d}V(z)}{\mathrm{d}z} \times \int_{M_{\rm lim}} \mathrm{d}M\, n(M,z)\,(\pi\theta_{\rm vir}^2)\right]\right\}, \tag{11}$$

where $n_{\rm ran}(\nu)$ is the surface number density of pure noise peaks without foreground DM haloes. It can be calculated with $\kappa^{(S)} = 0$, $\kappa_i^{(S)} = 0$ and $\kappa_{ij}^{(S)} = 0$.

We can see that, in the model, the cosmological information comes from the halo mass function, the internal density profile of DM haloes and the cosmological distances in the lensing efficiency factor as well as the cosmic volume element. This model has been tested extensively with simulations (Fan et al. 2010; Liu et al. 2014). In Appendix A, we further test the model performance with the simulations from Dietrich & Hartlap (2010) with different underlying cosmological parameters, and they have already been applied to derive cosmological constraints with observed WL peaks of CS82 and CFHTLenS data.

3.3 Map making

In this section, we present the map making procedure from the KiDS-450 shear catalogue. In order to build a reliable WL peak catalogue, three kinds of maps need to be generated for each tile.

(1) *Convergence map.* Using the observed shear catalogue of KiDS-450, the smoothed shear field at positions $\boldsymbol{\theta}$ can be calculated by taking into account the multiplicative and additive calibration corrections,

$$\langle \boldsymbol{\epsilon}_i \rangle(\boldsymbol{\theta}) = \frac{\sum_j W_{\theta_{\rm G}}(\boldsymbol{\theta}_j - \boldsymbol{\theta}) w(\boldsymbol{\theta}_j) \epsilon_i^c(\boldsymbol{\theta}_j)}{\sum_j W_{\theta_{\rm G}}(\boldsymbol{\theta}_j - \boldsymbol{\theta}) w(\boldsymbol{\theta}_j)(1+m_j)}, \tag{12}$$

where $W_{\theta_{\rm G}}$ is the Gaussian smoothing function in equation (2) with the smoothing scale $\theta_{\rm G} = 2$ arcmin, $\epsilon_i^c = \epsilon_i - c_i$, where ϵ_i and ϵ_i^c are the uncorrected and corrected ellipticity components, m and (c_1, c_2) are the multiplicative and the additive bias corrections, respectively, and w is the LENSFIT weight of source galaxy shape measurements. The summation is over galaxies j at positions $\boldsymbol{\theta}_j$.

For the KiDS-450 lensing data with redshift $0.1 < z_{\rm B} \leq 0.9$, the average multiplicative and additive biases (m, c) are quite small with $(\sim 1.4 \times 10^{-2}, \sim 3.9 \times 10^{-4})$, respectively. Given that the residual uncertainty in the bias estimation is only 1 per cent, it can only influence the theoretical predictions for peak counts with $\nu > 3$ by $\sim$1−2 per cent. This is well within the statistical uncertainties of our measurement.

The additive bias, c, is obtained empirically from the data by averaging the measured ellipticities in different KiDS patches and redshift bins. Their uncertainties are at the level of $\sim 6 \times 10^{-5}$. As discussed in Kacprzak et al. (2016), the additive bias systematics can vanish within the smoothing scale except for the galaxies at the edges of survey masks. With the filling factor cut in our peak analysis (see below), we expect a negligible impact of the additive bias on our results.

With the smoothed shear fields, the convergence map can be reconstructed iteratively for each individual tile using the non-linear KS inversion (Seitz & Schneider 1995; Liu et al. 2014). Assuming $\kappa^{(0)} = 0$ in a tile, we have $\gamma^{(0)} = \langle \boldsymbol{\epsilon} \rangle$. At the nth step, we can obtain $\kappa^{(n)}$ from $\gamma^{(n-1)}$. We then update γ to $\gamma^{(n)} = (1 - \kappa^{(n)})\langle \boldsymbol{\epsilon} \rangle$ for the next iteration. The reconstruction process is stopped when the converging accuracy of 10^{-6}, defined to be the maximum difference of the reconstructed convergence between the two sequential iterations, is reached.

(2) *Noise map.* To estimate the shape noise properties in each tile, the m-corrected ellipticity of each source galaxy is rotated by a random angle to destroy the lensing signal. Then following the same reconstruction procedures described above in (1), we can obtain the convergence noise field for each tile in KiDS-450.

(3) *Filling factor map.* Because mask effects can influence the WL peak counts significantly (Liu et al. 2014), the regions around masks should be excluded in the WL peak analysis. For that, we need to construct filling factor maps from the positions and weights of source galaxies. The filling factor is defined as the ratio of the true source galaxy density to that of the randomly populated galaxy distribution as follows:

$$f(\boldsymbol{\theta}) = \frac{\sum_j W_{\theta_{\rm G}}(\boldsymbol{\theta}_j - \boldsymbol{\theta}) w(\boldsymbol{\theta}_j)}{\langle \sum_n W_{\theta_{\rm G}}(\boldsymbol{\theta}_n - \boldsymbol{\theta}) \tilde{w}(\boldsymbol{\theta}_n) \rangle}. \tag{13}$$

Here the numerator is calculated from the observed galaxy positions $\boldsymbol{\theta}_j$ and weights $w(\boldsymbol{\theta}_j)$. The denominator is calculated by randomly populating galaxies over the full area of an extended tile. Specifically, we first find for each tile the average number density of galaxies in the area excluding the masked regions. We then randomly

populate galaxies over the full field of the extended tile including the masked regions. Each galaxy is then assigned a weight $\tilde{w}$ randomly according to the weight distribution of the source galaxies. From this random galaxy distribution, we obtain the denominator where the summation is over all galaxies.

With the filling factor maps, we can then identify and exclude regions around masks in the reconstructed convergence maps for peak counting. To control the systematic effects from the masks, we remove the regions with filling factor values $f < 0.6$ in the peak counting (Liu et al. 2014).

3.4 Peak identification

In a reconstructed convergence map, a peak is identified if its pixel value is higher than that of the 8 neighbouring pixels.

We exclude a tile entirely if its effective galaxy number density $n_{\rm eff} < 5.5$ arcmin^2 to ensure the validity of the Gaussian noise and the approximate uniformity of the noise field (Appendix B). After further rejecting the tiles that fail the filling factor requirement, the total area for the peak analysis is $\sim$304.2 deg^2.

We then divide peaks into different bins based on their SNR $\nu = \kappa/\sigma_0$, where σ_0 is the mean rms of the noise estimated from the noise maps considering only the regions that passed all requirements. With $\theta_{\rm G} = 2$ arcmin, we have $\sigma_0 \sim 0.023$. Due to limitations in the model, we only consider peaks with $\nu > 3$, corresponding to a smoothed $\kappa \gtrsim 0.07$. For higher SNR, we include those bins that contain at least 10 peaks to avoid the bias resulting from the large Poisson fluctuations. We thus concentrate on the peaks in the range of $3 < \nu < 5$.

3.5 Fitting method

We use the model described in Section 3.2 to derive cosmological constraints from the observed WL peaks identified from the convergence maps. We divide the measurements into four equally wide SNR bins ([3.0, 3.5], [3.5, 4.0], [4.0, 4.5], [4.5, 5.0]), where the number of peaks in the last bin being $\sim$10 and significantly larger in the other bins. We define the following χ^2 to be minimized for cosmological parameter constraints,

$$\chi^2_p = \sum_{i,j=1}^{4} \Delta N_i^{(p)} (\widehat{C_{ij}^{-1}}) \Delta N_j^{(p)}, \tag{14}$$

where $\Delta N_i^{(p)} = N_{\rm peak}^{(p)}(\nu_i) - N_{\rm peak}^{(d)}(\nu_i)$ is the difference between the theoretical prediction with cosmological model p and the observed peak counts. The covariance matrix C_{ij} is estimated from bootstrap analysis by resampling the 454 tiles from the KiDS-450 data, and is given by

$$C_{ij} = \frac{1}{R-1} \sum_{r=1}^{R} [N_{\rm peak}^{r}(\nu_i) - N_{\rm peak}^{(d)}(\nu_i)][N_{\rm peak}^{r}(\nu_j) - N_{\rm peak}^{(d)}(\nu_j)]. \tag{15}$$

Here, r denotes different bootstrap samples with the total number $R = 10\,000$, and $N_{\rm peak}^{r}(\nu_i)$ is the peak count in the bin centred on ν_i from sample r. The unbiased inverse of the covariance matrix can then be estimated as (Hartlap, Simon & Schneider 2007)

$$\widehat{\mathbf{C}^{-1}} = \frac{R - N_{\rm bin} - 2}{R-1} (\mathbf{C}^{-1}), \quad N_{\rm bin} < R - 2, \tag{16}$$

where $N_{\rm bin}$ is the number of bins used for peak counting. In our analysis, we adopt the bootstrap covariance estimated from the KiDS-450 data. Liu et al. (2015b) found that the differences between the results from simulation sets and from bootstrap resampling are generally less than 10 per cent for the diagonal elements of the inverse.

With $N_{\rm bin} = 4$, in this paper, we consider constraints on the most lensing-sensitive parameters ($\Omega_{\rm m}$, σ_8) under the flat Λ cold dark matter (ΛCDM) assumption. In our fiducial analysis, the other parameters including the Hubble constant h, the power index of the initial density perturbation spectrum $n_{\rm s}$ and the present baryonic matter density $\Omega_{\rm b}$ are fixed to $h = 0.7$, $n_{\rm s} = 0.96$ and $\Omega_{\rm b} = 0.046$. We also consider the cases with different Hubble constant to see if this uncertainty can affect the results significantly. Our Markov chain Monte Carlo (MCMC) fitting uses COSMOMC (Lewis & Bridle 2002) modified to include the likelihood of WL peak counts. We adopt flat priors in the range of [0.05, 0.95] and [0.2, 1.6] for $\Omega_{\rm m}$ and σ_8, respectively.

In Appendix A, we further test the model performance by comparing with simulations from Dietrich & Hartlap (2010) of different ($\Omega_{\rm m}$, σ_8). In Appendix C, we analyse KiDS-450-like mock data based on our own simulations using the full peak analysis pipeline. It is shown that the derived constraints from the mock data can recover the input cosmological parameters very well.

4 SYSTEMATICS

As discussed in previous sections, the measurement systematics, including the shear measurement bias and photo-z errors, are negligible for our KiDS-450 WL peak analysis. However, we need to further understand the impact of astrophysical systematic effects, such as the boost factor due to cluster member contamination and the blending in cluster regions, baryonic effects, the projection effects of LSS and IA of galaxies.

4.1 Boost factor

The true high-SNR peaks that we detect are mainly due to individual massive clusters. Cluster member contamination to the source galaxy catalogue can however dilute the lensing signals (e.g. Mandelbaum et al. 2006; Miyatake et al. 2015; Dvornik et al. 2017). In addition, the galaxies in cluster regions can be blended because of galaxy concentration, resulting in lower shear measurement weights. Both these effects need to be accounted as a 'boost factor' (Kacprzak et al. 2016).

With DES-SV data, Kacprzak et al. (2016) find that the boost factor correction is <5 per cent for their shear peak studies: the dilution of the signal by cluster member galaxies is minimal (<2 per cent), and the effect of background galaxies lost because of blending is $\sim$5 per cent in the SNR of the highest SNR peaks with $3.66 \leq \nu \leq 4.0$ with aperture radius $\theta_{\rm max} = 20$ arcmin. We note that our peak analysis is different from that of Kacprzak et al. (2016 , convergence versus shear peaks, and Gaussian filter versus NFW-like filter). The modelling of the cosmological dependence is also different (theoretical versus simulation templates). Thus, the estimate of the boost factor of Kacprzak et al. (2016) may not be directly applicable here. In this section, we estimate the boost effect based on our analysis, drawing out the different conclusions to Kacprzak et al. (2016).

The boost factor effect on peak statistics results from the excess galaxy number density (filling factor) of source galaxies near massive clusters, compared to the average number density. To estimate these differences, it is better to analyse the source galaxies near known clusters in the field rather than around peaks because a considerable fraction of peaks are non-halo-associated.

In the galaxy–galaxy lensing measurement with KiDS and GAMA data, Dvornik et al. (2017) find that the member contamination for GAMA groups can reach up to ∼30 per cent at 75 kpc h^{-1} and decreases on larger scales. In our analysis, we use a Gaussian smoothing with $\theta_G = 2$ arcmin. This corresponds to a scale of ∼300 kpc h^{-1} at redshift ∼0.2–0.3. Then a member contamination of ∼10 per cent is expected. On the other hand, GAMA groups have a typical mass of $10^{13}\,M_\odot\,h^{-1}$ (Dvornik et al. 2017), smaller compared to those responsible for the high-SNR peaks.

We therefore use the cluster candidates from Radovich et al. (2017) found in 114 deg^2 of KiDS regions. The mass of the cluster candidates is estimated using the richness as a proxy (Anderson 2015). To assess the boost factor effect due to the member contamination and the blending effect in cluster regions, similar to Kacprzak et al. (2016), we analyse the filling factor of source galaxies near these cluster candidates. Specifically, in accord with the high-SNR peak studies, we consider clusters with mass $M > 10^{14}\,h^{-1}\,M_\odot$. In Appendix D, we quantify the impact of the boost factor effects on both the signal and the noise level for WL peak counts from KiDS-450 data. They can affect the peak abundance by ∼(−2.0 per cent, −6.0 per cent, −14.0 per cent, −27.0 per cent) on the four SNR bins ([3.0, 3.5], [3.5, 4.0], [4.0, 4.5], [4.5, 5.0]) for the best-fitting cosmology. We include the boost factor effect in our fiducial analysis to derive cosmological parameter constraints (see Section 5).

4.2 Baryonic effects

Although baryonic matter is subdominant compared to DM, it is subject to complicated physical processes such as heating, cooling and feedback from stars and AGNs, all of which can have significant influence on structure formation. For the WL peak analysis, the baryonic effect can be estimated by how it changes the DM distribution in haloes.

Using a simplified model for the cooling and condensation of baryons at the centres of DM haloes, Yang et al. (2013) claim that there is a large increase in the number of high-SNR peaks, but the effects on low-SNR peaks are quite small.

On the other hand, including the feedback of supernovae, stars and AGNs, Osato et al. (2015) find that the feedback effects can effectively reduce the mass of small DM haloes, eventually reducing the number of low-SNR WL peaks. Because of the smaller impact of feedback on the massive DM haloes (Velliscig et al. 2014), the high-SNR peak number is not significantly changed. Osato et al. (2015) also show that the high-SNR peaks are almost unaffected once all the contributions from radiative cooling and the various feedbacks are included, because these effects can partially compensate each other. In fact, the baryonic effects are only expected to generate 1−2 per cent biases on the (Ω_m, σ_8) constraints from high-SNR peak analysis (Osato et al. 2015).

Studies of the baryonic effects on WL peak statistics have not yet reached an agreement. This is mainly due to the different physical processes considered in the different analyses. Because the details of the baryonic physics are complicated and remain to be fully understood, it would be highly valuable if we could obtain some constraints on them from observations simultaneously with cosmological parameters. In addition, a self-calibrated method can also reduce biases on cosmological parameter constraints arising from improper assumptions about the baryonic sector. In our theoretical modelling, the dependence of WL peak counts on baryonic effects is explicit. It is therefore possible for us to carry out studies including self-calibration.

For high-SNR WL peak counts, it is a reasonable assumption that baryonic effects show up through modifying the density distribution of DM haloes (Duffy et al. 2010; Mead et al. 2015). We therefore include some freedom in the halo mass–concentration relation. Specifically, we take the power-law form of the mass–concentration relation for NFW haloes,

$$c_{\rm vir} = \frac{A}{(1+z)^{0.7}}\left(\frac{M_{\rm vir}}{10^{14}\,h^{-1}\,M_\odot}\right)^{\beta}, \tag{17}$$

where $A = 5.72$ and $\beta = -0.081$ are given in Duffy et al. (2008). The redshift dependence $(1+z)^{0.7}$ is taken to be consistent with simulation results (Duffy et al. 2008; Bhattacharya et al. 2013). In order to quantify the possible baryonic effects on the density profiles and also the impact of the uncertainties of the mass–concentration relation, we allow the amplitude A to be a free parameter in our fiducial analysis. With a wide flat prior of [0, 20], we then perform the simultaneous constraints on the cosmological and structural parameters (Ω_m, σ_8, A, see Section 5). Comparing with the prediction of DM-only simulations, the derived A tends to be somewhat higher. But the current peak counts can hardly put any meaningful constraints on A.

4.3 The projection effects of LSS

Previous studies have shown that WL peaks of different SNR originate from different sources (Yang et al. 2011; Liu & Haiman 2016). While high-SNR peaks originate primarily from individual massive DM haloes (see Section 33), low-SNR peaks often result from the cumulative contributions of the LSS along the LOS.

However, the projection effects of LSS affect the measurements of peaks for all SNR (Hoekstra 2001; Hoekstra et al. 2011). With the model of Fan et al. (2010), Yuan et al. (2017) investigate in detail the projection effects of LSS on high-SNR peaks, which shows that the ratio $\sigma^2_{0,\rm LSS}/\sigma^2_0$ can give a rough estimate of the importance of LSS in comparison with that of the shape noise, where $\sigma_{0,\rm LSS}$ is the rms of the smoothed convergence field from LSS excluding the massive halo contributions and σ_0 is the rms of the residual shape noise. The higher the redshift and the larger the density of source galaxies, the more important the effect of LSS. For KiDS-450, the number density is relatively low and thus the shape noise is large. The median redshift is also relatively low with ∼0.65. In this case, $\sigma^2_{0,\rm LSS}/\sigma^2_0 \sim (0.006/0.023)^2 \sim 0.07$, and thus the LSS effect is much lower than that of the shape noise. Furthermore, the effective area used in our peak analysis is ∼300 deg^2, and the statistical errors of peak counts are relatively large. We therefore expect minor impacts of LSS in our current analysis.

In fact, the projection effects of LSS are naturally included in the mock simulation data. The unbiased results of the cosmological constraints from the mocks (Appendix C) suggest that the LSS projection effects are indeed negligible and the model that does not account for LSS projections still provides a good fit to the mock data. We note that for KiDS, with the increase of the survey area, the statistical errors of peak counts will decrease and the tolerable levels of systematic errors will also decrease. Thus, the LSS effect may need to be included in the peak modelling in future analysis (Yuan et al. 2017).

Moreover, by comparing with simulation templates, the low-SNR shear peaks from the projection effects of LSS are used to probe the cosmological information in Paper II.

4.4 Intrinsic alignments

The IA signal of galaxies contains important information on the formation and evolution of galaxies in their DM environment. For the cosmic shear 2PCF measurements, the IA effects can be divided into two components: the intrinsic ellipticity correlations and shear-ellipticity correlations. They can contaminate the cosmic shear analysis.

Fan (2007) studied the influence of IA on the convergence peak counts, by modelling it as additional terms to the moments of the shape noise. The full noise variance in a convergence map can then be written as $\sigma_0^2 = \sigma_{0,\mathrm{ran}}^2 + \sigma_{0,\mathrm{corr}}^2$, where $\sigma_{0,\,\mathrm{ran}}$ is the noise contributed from the randomly oriented intrinsic ellipticities of source galaxies and $\sigma_{0,\,\mathrm{corr}}$ denotes the additional contribution from IA (see equation 23 in Fan 2007). For the KiDS-450 data, we have $\sigma_{0,\mathrm{ran}}^2 = 0.023^2 = 5.3 \times 10^{-4}$ with a 2 arcmin Gaussian smoothing. We can estimate $\sigma_{0,\mathrm{corr}}^2 < 3.07 \times 10^{-6}$ with the IA amplitude $A_{\mathrm{IA}} = 1.10 \pm 0.64$ from the cosmic shear constraints (Hildebrandt et al. 2017), which is much smaller than $\sigma_{0,\mathrm{ran}}^2$.

Apart from contributing to the noise variance, IA can also affect the peak signal estimates. If there is a contamination of cluster members to the source catalogue and these members are intrinsically aligned to the centre, the estimated lensing signal would be biased. Using a simple model of radial alignment of satellite galaxies with a certain misalignment angle consistent with simulations, Kacprzak et al. (2016) estimated the IA influence on the SNR of shear peaks with the aperture mass statistics. They find that the IA effects can be important for high-SNR shear peaks. For peaks with SNR $\nu > 4.5$, the number of shear peaks can change by about 30 per cent.

On the other hand, observationally, Chisari et al. (2014) find that the IA signals in stacked clusters of the Sloan Digital Sky Survey 'Stripe 82' in the redshift range $0.1 < z < 0.4$ are consistent with zero. Using a large number of spectroscopic members of 91 massive galaxy clusters with a median redshift $z_{\mathrm{med}} \sim 0.145$, Sifón et al. (2015) also find that the IA signal of cluster members is consistent with zero for all scale, colour, luminosity and cluster mass investigated. Because high-SNR peaks are mainly due to individual massive DM haloes hosting clusters of galaxies, these observational results may indicate negligible IA effects for high-SNR peak signal estimates.

We further note that for our analysis here, the number of peaks with SNR > 4.5 is about 10, for which the Poisson statistical uncertainty reaches ∼33 per cent. For such large statistical fluctuations, we do not expect the IA contamination to matter.

To summarize, the measurement systematics (shear measurement bias and photo-z errors) and some astrophysical systematic effects (the projection effects of LSS and IA) are insignificant for our cosmological studies using WL peaks from KiDS-450, and will be neglected. On the other hand, in our fiducial studies, we include the boost effect, which we find to be significant. We also allow the amplitude of the halo mass–concentration relation to vary to account for possible baryonic effects.

5 COSMOLOGICAL CONSTRAINTS FROM KIDS-450 PEAK ANALYSIS

In this section, we present cosmological constraints derived from the KiDS-450 WL peak analysis, incorporating both the boost factor and baryonic effects as discussed in Section 4.

First, we show the peak counts from KiDS-450 in the upper panel of Fig. 1. The data are shown as points, their error bars have been calculated using a bootstrap sampling of individual KiDS-450 observation tiles, and the solid line is our best-fitting theoretical model. The lower panel shows the residual between the data and this prediction. The corresponding peak numbers are also shown in Table 1. Secondly, Fig. 2 shows our fiducial constraints on Ω_{m} and σ_8 in comparison with the results from the KiDS-450 cosmic shear tomographic 2PCF analysis (Hildebrandt et al. 2017). In addition, we show the pre-*Planck* CMB constraints (*WMAP*9+ACT+SPT; Calabrese et al. 2017) and the *Planck* CMB constraints 'TT+lowP' (Planck Collaboration XIII 2016a).

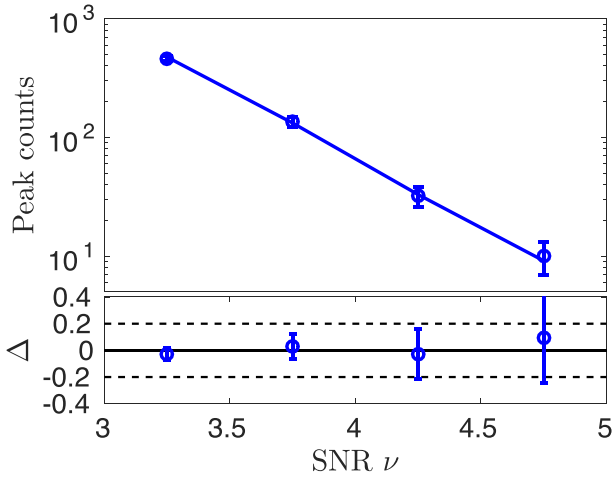

Figure 1. Upper panel: the fiducial peak count distribution of the KiDS-450 data. The corresponding solid line is the theoretical prediction with the best-fitting cosmological parameters obtained from MCMC fitting. The error bars are the square root of the diagonal terms of the covariance matrix. Lower panel: the difference between the peak counts of the data and the best-fitting theoretical predictions.

Table 1. The peak counts from the KiDS-450 data and of the theoretical predictions from the best-fitting cosmological model in our fiducial analyses.

	$N_{\mathrm{peak}}^{\mathrm{data}}$	$N_{\mathrm{peak}}^{\mathrm{fid}}$
$3.0 \le \nu < 3.5$	462 ± 23	475.04
$3.5 \le \nu < 4.0$	136 ± 13	132.11
$4.0 \le \nu < 4.5$	32 ± 6	32.96
$4.5 \le \nu < 5.0$	10 ± 3	9.12

From Figs 1 and 2, we can see that the results from our WL peak analysis are an accurate representation of the KiDS-450 data, and that they are consistent with the cosmological constraints reported using a 2PCF analysis of the same data set. Both methods return constraints that agree well with pre-*Planck* CMB measurements. Furthermore, it can be seen that the degeneracy relation has a somewhat flatter slope than that from tomographic 2PCF measurements. This difference means that our analysis has great potential to be used in a manner that is complementary to cosmic shear correlation analysis, as a joint analysis may provide tighter cosmological constraints than is possible with either analysis alone.

Finally, comparison with *Planck* CMB measurements reveals a tension similar to that reported in previous KiDS studies. This tension is quantified in the following section.

5.1 Comparison of S_8 values

Due to the strong degeneracy between Ω_{m} and σ_8 from WL analyses, cosmological constraints are often characterized via the single

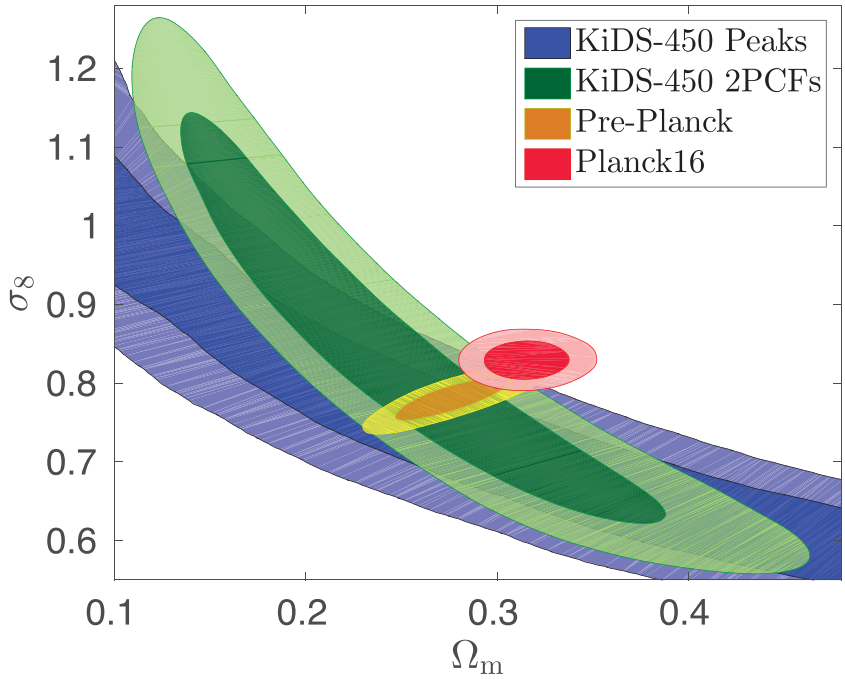

Figure 2. The comparison for the constraints on (Ω_m, σ_8) between the fiducial WL peak analysis (blue) and the results from the cosmic shear tomography from KiDS-450 (green). The constraints from pre-*Planck* CMB measurement (yellow) and *Planck* 2016 (red) are also overplotted. The contours are 1σ and 2σ confidence levels, respectively.

quantity $\Sigma_8 = \sigma_8(\Omega_m/0.3)^\alpha$, where the index α is indicative of the slope of the degeneracy direction. When performing cosmic shear 2PCF analyses, this degeneracy is typically found to have a slope of $\alpha \sim 0.5$. As such, Σ_8 is frequently re-defined as $S_8 = \sigma_8(\Omega_m/0.3)^{0.5}$. In either case, with a freely varying or fixed value α, this characterization parameter can be constrained better than Ω_m and σ_8 separately. Given the frequent use of S_8 rather than Σ_8 in the literature, we first calculate S_8 and subsequently calculate Σ_8, fitting for the free parameter α.

Using our fiducial WL peak analysis, we find $S_8 = 0.746^{+0.046}_{-0.107}$. This value is in agreement with that from cosmic shear tomographic 2PCF analysis, which gives $S_8 = 0.745^{+0.039}_{-0.039}$ (Hildebrandt et al. 2017). To show the robustness of the results, we explore the impact (on our estimated S_8) of the various systematic effects that were accounted for in our model, and of some systematic effects external to our model. After these tests, we then also compare our S_8 estimates to additional constraints from the literature.

5.1.1 *Testing systematic effects*

We first ignore all the measurement and astrophysical systematics, and estimate S_8 in the absence of our boost factor and baryonic effect corrections. This allows us to obtain a no-systematics estimate of $S_8 = 0.748^{+0.038}_{-0.146}$. This value is included in Fig. 3, and is indicative of how our estimate of S_8 changes under consideration of these two systematic effects. Interestingly, we can see that our fiducial measurement of S_8 is largely unchanged here. This is because of the compensation of the boost effect and the baryonic effect to be shown in the following. We also note that, for both of these estimates (and in fact for all our estimates of S_8), the error bars are strongly asymmetric. This is due primarily to the different degeneracy direction compared with the assumed slope of $\alpha = 0.5$. Indeed, fitting with a free α results in a much more symmetric uncertainty estimate (see Section 5.2). Moreover, the seemingly larger error bars in the case of no systematics are mainly due to the different degeneracy direction from $\alpha = 0.5$. With the fitting α, the probability distribution of Σ_8 is much more symmetric and the errors are indeed smaller in the no-systematics case than that of our fiducial analyses.

Considering only the boost effect, with the modified model described at length in Appendix D, we find $S_8 = 0.782^{+0.043}_{-0.124}$. This shows that the boost factor pushes S_8 to higher values, and leads to a marginal reduction in uncertainty.

Testing the influence of baryonic effects by freeing the A parameter without including the boost effect, we find $S_8 = 0.720^{+0.042}_{-0.133}$. This is made by marginalizing over A, and is also shown in Fig. 3. This estimate is ∼3.8 per cent lower than the no-systematics value, and is marginally higher than might be expected from previous simulation studies (see e.g. Osato et al. 2015). None the less, the effect is minor. However, it is relevant to note that in the future this will not be the case. Future large WL surveys will provide sufficient area that WL peak counts will increase by order of magnitude. We expect that our self-calibration method will be particularly useful, allowing both a significant reduction in cosmological parameter constraint biases and valuable information about baryonic physics.

The above analyses show that the two systematics move the S_8 estimate in opposite directions. As a result, when both are considered in our fiducial analyses, their effects are largely cancelled out and the S_8 value is nearly unchanged comparing to the case of no systematics.

We also assess the impact of redshift uncertainties. To do this, we carry out the peak analysis using the posterior redshift distribution $P(z)$ returned by BPZ. Here we do not include the boost factor and baryonic effects, and our results are compared to our no-systematics estimate. This test returns a value $S_8 = 0.773^{+0.044}_{-0.139}$, and is shown in Fig. 3 as KiDS-450 peak (BPZ). This S_8 estimate is marginally higher than our no-systematics analysis, primarily because the mean of BPZ redshift distribution is lower than that of DIR. This is in agreement

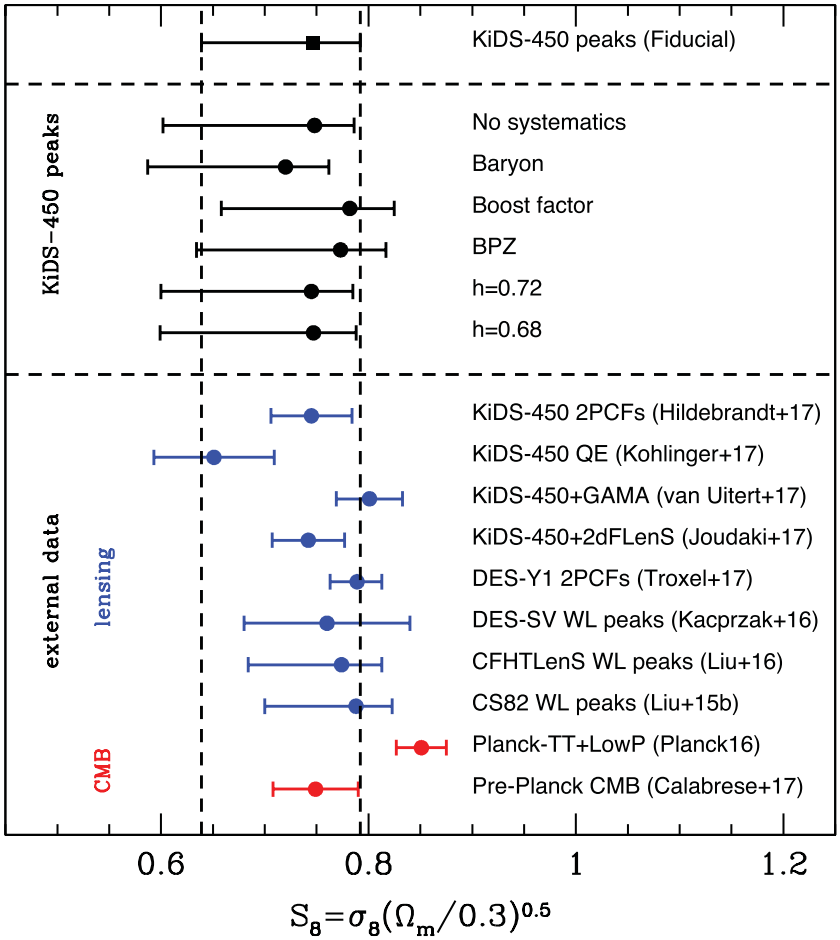

Figure 3. Constraints on S_8 from our WL peak analysis, including various systematic tests, compared to various estimates from the literature measurements.

with the analysis of Hildebrandt et al. (2017), who observe a similar effect in cosmic shear constraints of S_8.

We also test how sensitive our estimate of S_8 is to the variation of the mean redshift of the bootstrapped DIR sample. We select the two bootstrap realizations with the most different mean estimates comparing to the one used in our main studies. Specifically, the difference in the mean redshift is $\Delta\langle z\rangle = +0.036$ and $\Delta\langle z\rangle = -0.037$, respectively. Correspondingly, the obtained values of S_8 are $S_8 = 0.744^{+0.039}_{-0.147}$ and $0.750^{+0.039}_{-0.136}$, respectively. The results are consistent with our no-systematics estimate within the statistical errors, indicating a negligible bias from the DIR photo-z uncertainties.

Finally, in our analysis we have assumed a reduced Hubble constant $h = 0.7$. However, recent results from *Planck* CMB temperature and polarization analyses suggest that h may be smaller than our assumed value. To estimate the effect of a change in h on our results, we perform two additional measurements of S_8 assuming $h = 0.68$ and 0.72. For the no-systematic cases, the derived parameters are $S_8 = 0.747^{+0.041}_{-0.148}$ and $0.745^{+0.040}_{-0.145}$, for $h = 0.68$ and 0.72, respectively. Again, these results are consistent with our fiducial estimate and indicate that our results are robust to modest variations in h.

5.1.2 *External constraints*

When comparing our S_8 constraints with those from previous CMB temperature and polarization measurements, we find very good agreement with pre-*Planck* CMB-based constraints from Calabrese et al. (2017). However, similar to the tomographic 2PCF analyses, our result is lower than the CMB measurement from *Planck* ($S_8 = 0.851 \pm 0.024$; Planck Collaboration XIII 2016a) at the level of $\sim 2.0\sigma$. Fig. 3 shows these results and those from other KiDS-450 measurements, the Dark Energy Survey Year One (DES-Y1) cosmic shear measurement, and previous WL peak analyses, in comparison to our fiducial estimate and our various systematic tests from Section 5.1.1.

Our estimate of S_8 is consistent with all previous KiDS analyses, within 1σ uncertainties. To demonstrate this, we highlight the following results in particular. Köhlinger et al. (2017) use power spectrum analysis to estimate S_8, finding $S_8 = 0.651 \pm 0.058$. Combining cosmic shear measurements from KiDS-450 with galaxy–galaxy lensing and angular clustering from GAMA, van Uitert et al. (2017) obtained $S_8 = 0.801 \pm 0.032$. In a parallel analysis, Joudaki et al. (2017b) found $S_8 = 0.742 \pm 0.035$ using KiDS-450 cosmic shear measurements with galaxy–galaxy lensing and redshift space distortion from the 2-degree Field Lensing Survey (Blake et al. 2016) and the Baryon Oscillation Spectroscopic Survey (Dawson et al. 2013).

Moreover, our estimate of S_8 is also consistent with the recent results from DES-Y1. Troxel et al. (2017) report a cosmic shear-based estimate of $S_8 = 0.789^{+0.024}_{-0.026}$, which is again in good agreement with the value presented here.

We also compare our results to previous WL peak analyses in the literature, finding good agreement. Liu et al. (2015b) use CS82

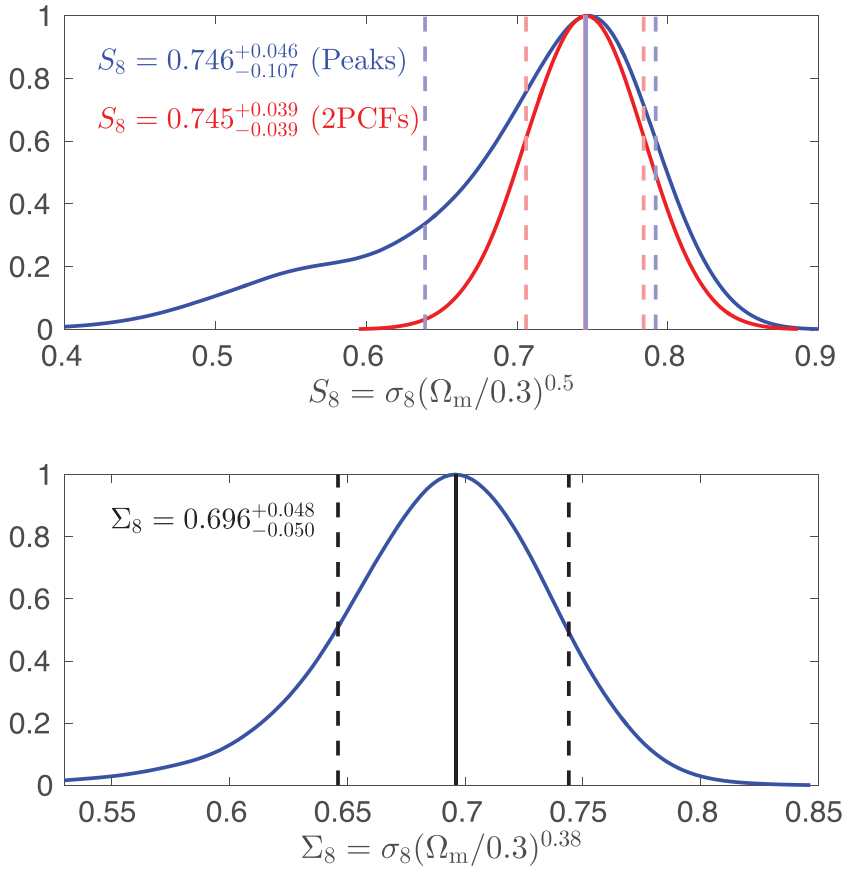

Figure 4. Upper panel: the marginalized probability distribution of S_8 for KiDS-450 WL peak statistics (blue) and the cosmic shear tomographic 2PCF analysis (red). Lower panel: the marginalized distribution of Σ_8 for KiDS-450 WL peak statistics.

data and find $S_8 = 0.788^{+0.035}_{-0.088}$. They also fit for a free α, finding a lower value than $\alpha = 0.5$ assumed by S_8. Liu et al. (2016) use CFHTLenS to constrain $f(R)$ theory using WL peak statistics. While they do not report S_8 directly, we are able to utilize their WL peak catalogue to estimate S_8 for their sample, finding $S_8 = 0.774^{+0.039}_{-0.090}$. Finally, Kacprzak et al. (2016) use DES-SV to study the abundance of shear peaks with $0 < \nu < 4$, identified in aperture mass maps. They constrain cosmological parameters using a suite of simulation templates with 158 models with varying (Ω_m, σ_8) (Dietrich & Hartlap 2010). They find $S_8 = 0.76 \pm 0.074$, with uncertainty derived by marginalizing over the shear multiplicative bias and the error on the mean redshift of the galaxy sample. The constraints from these studies are marginally higher than our results, while being none the less consistent with our fiducial result within uncertainties.

We conclude that our results are consistent with the pre-*Planck* CMB measurement of Calabrese et al. (2017), other KiDS-450 measurements, DES-Y1 cosmic shear and other WL peak analyses. The $\sim 2.0\sigma$ tension with *Planck* CMB measurements is again seen here.

5.2 Parameter degeneracy

As shown in Fig. 2, our (Ω_m, σ_8) degeneracy direction is somewhat flatter than that present in 2PCF analyses. This difference, we argue, results in significantly asymmetric uncertainties on our estimate of S_8. We demonstrate this clearly in the upper panel of Fig. 4, where we show the marginalized probability distribution of S_8 for our fiducial WL peak analysis (blue) and cosmic shear tomographic 2PCF analysis (red). Our distribution is clearly heavily skewed, with a long tail towards the lower values of S_8.

As this tail is clearly an artefact caused by the use of a fixed $\alpha = 0.5$, we now explore how our estimates change when we fit with a freely varying α; that is, we fit for Σ_8 rather than S_8. We derive the best-fitting $\alpha \approx 0.38$ using the values of (Ω_m, σ_8) that are within 1σ confidence level of the constraints (the dark blue region in Fig. 2). The smaller α reflects the flatter contours from our peak analyses than that from 2PCFs, consistent with the visual inspections. With the fitted α, we then calculate the distribution of Σ_8 from the obtained constraints on (Ω_m, σ_8). The result is shown in the lower panel of Fig. 4. It is seen that the distribution is significantly more symmetric than the distribution of S_8. With the best-fitting α, our final estimate is $\Sigma_8 = 0.696^{+0.048}_{-0.050}$.

We note that our constraint on α is similar to that recovered from cluster count analyses (Vikhlinin et al. 2009; Rozo et al. 2010; Planck Collaboration XXIV 2016b). These all find smaller α although they vary somewhat: Vikhlinin et al. (2009) find $\alpha \approx 0.47$ from analyses of X-ray clusters; Rozo et al. (2010) find $\alpha \approx 0.41$ using MaxBCG analysis; and studies of Sunyaev-Zel'dovich (SZ) clusters find $\alpha \approx 0.3$ (Planck Collaboration XXIV 2016b). The variations could be due to systematically different masses and redshifts probed by these different studies. It is interesting to note that the non-tomography high-SNR shear peak analyses of Dietrich & Hartlap (2010) with simulation templates also obtain a flatter degeneracy direction. Each of these studies is broadly consistent with our best-fitting $\alpha \sim 0.38$, which is expected due to the significant correlation between high-SNR WL peaks and massive clusters of galaxies.

6 CONCLUSIONS

We derive cosmological constraints from a WL peak count analysis using 450 deg^2 of KiDS data. As shape noise is the dominant source of uncertainties in our analysis, we adopt the theoretical model of Fan et al. (2010), which takes into account the various effects of shape noise in modelling peak counts.

We begin by testing the applicability of this model. Comparing its predictions with WL peak counts from simulations of different cosmologies (Appendix A), we find good agreement between the model and our simulations. We also test the Gaussian approximation for the residual shape noise used in the model (Appendix B), again finding consistent results. Finally, we perform a mock KiDS analysis using a suite of simulations to validate our full analysis pipeline (Appendix C), finding that our pipeline recovers the input cosmology consistently.

After verifying both the model and our pipeline, we estimate our 'fiducial' cosmological constraints using the DIR calibrated redshift distribution (Hildebrandt et al. 2017) and high-SNR peaks ($3 < \nu < 5$), accounting for the influence of boost factor and baryonic effects. We explore other systematics, including projection effects of LSS, shear measurement bias and photo-z errors, and conclude that these are insignificant for the WL peak analysis performed here. We explore the effect of IA, finding it to have negligible impact on shape noise variance and therefore on our results. However, considering the cluster member contamination, we find that the peak signal measurements may be affected if member galaxies have IA within clusters. The existence of such alignments is, however, still debated within the literature; we opt not to include it in our analysis. Further study of the effects of IA is none the less of interest, and we leave this for future work.

We summarize our primary conclusions as follows.

(1) For a flat ΛCDM cosmology, our fiducial cosmological constraint on (Ω_m, σ_8) from WL peaks is $S_8 = \sigma_8(\Omega_\mathrm{m}/0.3)^{0.5} = 0.746^{+0.046}_{-0.107}$. This is consistent with previous estimates, within KiDS, from cosmic shear tomographic 2PCF analysis and shear peak counts. Our estimate is also consistent with previous WL peak studies from CFHTLenS, CS82 and DES-SV. Finally, our result is consistent with pre-*Planck* CMB results, although we find a tension of $\sim 2.0\sigma$ with the *Planck* CMB.

(2) We perform a quantitative analysis of a range of systematic effects, including photo-z errors and uncertainty in the Hubble constant h, finding that these are insignificant compared to the statistical uncertainties on our value of S_8.

(3) We fit for the degeneracy slope of (Ω_m, σ_8) from our high-SNR peak studies, characterized by the index α, finding a slope somewhat flatter than that found using cosmic shear 2PCF analysis. This raises the potential for WL peak analysis to be used alongside a 2PCF analysis, thereby breaking part of the (Ω_m, σ_8) degeneracy. Fitting for our cosmological constraint with α as a free parameter, we find $\Sigma_8 = \sigma_8(\Omega_\mathrm{m}/0.3)^\alpha = 0.696^{+0.048}_{-0.050}$, with the best-fitting $\alpha = 0.38$.

Previous estimates of α using low- and medium-SNR shear peaks (Kacprzak et al. 2016) find a degeneracy direction similar to that of cosmic shear 2PCF measurements. We argue that the primary complementarity with 2PCF studies, therefore, lies in studying high-SNR peaks. However, as the number of high-SNR peaks is still relatively low, even in our 450 deg^2 sample, the statistical uncertainties remain considerably larger than those of low-SNR peaks. Future WL surveys, such as *Euclid* (Laureijs et al. 2011), LSST (Abell et al. 2009) and the Wide Field Infrared Survey Telescope[7], will provide considerably larger samples of high-SNR peaks, and thus allow us to extract much more cosmological information from studies of this nature. However, achieving higher accuracy will come at a cost: much tighter control on systematic effects will be paramount.

ACKNOWLEDGEMENTS

We are thankful for the referee's encouraging comments and suggestions. The analyses are based on data products from observations made with ESO Telescopes at the La Silla Paranal Observatory under programme IDs 177.A-3016, 177.A-3017 and 177.A-3018, and on data products produced by Target/OmegaCEN, INAF-OACN, INAF-OAPD and the KiDS production team, on behalf of the KiDS consortium. OmegaCEN and the KiDS production team acknowledge support by NOVA and NWO-M grants. Members of INAF-OAPD and INAF-OACN also acknowledge the support from the Department of Physics & Astronomy of the University of Padova and of the Department of Physics of Univ. Federico II (Naples). We thank Antony Lewis for the COSMOMC packages. HYS acknowledges support from TR33 project 'The Dark Universe' funded by the DFG. HHi is supported by an Emmy Noether grant (No. Hi 1495/2-1) of the DFG. XKL, CZP and ZHF are supported in part by the NSFC of China under grants 11333001 and 11173001 and by Strategic Priority Research Program 'The Emergence of Cosmological Structures' of the Chinese Academy of Sciences, grant No. XDB09000000. XKL also acknowledges the support from General Financial Grant from China Postdoctoral Science Foundation with Grant No. 2016M591006. HHo acknowledges support from Vici grant 639.043.512, financed by the Netherlands Organisation for Scientific Research (NWO). JHD acknowledges support from the European Commission under a Marie-Sklodwoska-Curie European Fellowship (EU project 656869). CH acknowledges support from the European Research Council under grant number 647112. KK acknowledges support by the Alexander von Humboldt Foundation. JM has received funding from the European Union's FP7 and Horizon 2020 research and innovation programmes under Marie Sklodowska-Curie grant agreement numbers 627288 and 664931. QW acknowledges the support from NSFC with Grant No. 11403035. Part of the *N*-body simulations are performed on the Shuguang cluster at Shanghai Normal University, Shanghai, China.

REFERENCES

Abell P. A. et al., 2009, preprint (arXiv:0912.0201)
Aihara H. et al., 2017, PASJ, preprint (arXiv:1702.08449)
Anderson S., 2015, A&A, 582, A100
Angulo R. E., Springel V., White S. D. M., Jenkins A., Baugh C. M., Frenk C. S., 2012, MNRAS, 426, 2046
Bartelmann M., Schneider P., 2001, Phys. Rep., 340, 291
Benitez N., 2000, ApJ, 536, 571
Bhattacharya S., Habib S., Heitmann K., Vikhlinin A., 2013, ApJ, 766, 32
Blake C. et al., 2016, MNRAS, 462, 4240
Calabrese E. et al., 2017, Phys. Rev. D, 95, 063525
Chisari N. E., Mandelbaum R., Strauss M. A., Huff E. M., Bahcall N. A., 2014, MNRAS, 445, 726
Dawson K. et al., 2013, AJ, 145, 10
de Jong J. et al., 2015, A&A, 582, 62
de Jong J. et al., 2017, A&A, 604, A134

[7] http://wfirst.gsfc.nasa.gov/

Dietrich J. P., Hartlap J., 2010, MNRAS, 402, 1049
Duffy A. R., Schaye J., Kay S. T., Dalla Vecchia C., 2008, MNRAS, 390, L64
Duffy A. R., Schaye J., Kay S. T., Dalla Vecchia C., Battye R. A., Booth C. M., 2010, MNRAS, 405, 2161
Dvornik A. et al., 2017, MNRAS, 468, 3251
Erben T. et al., 2009, A&A, 493, 1197
Erben T. et al., 2013, MNRAS, 433, 2545
Falco E. E., Gorenstein M. V., Shapiro I. I., 1985, ApJ, 289, L1
Fan Z. H., 2007, ApJ, 669, 10
Fan Z. H., Shan H. Y., Liu J. Y., 2010, ApJ, 719, 1408
Fenech Conti I., Herbonnet R., Hoekstra H., Merten J., Miller L., Viola M., 2017, MNRAS, 467, 1627
Fu L., Fan Z. H., 2014, Res. Astron. Astrophys., 14, 1061
Hamana T., Takada M., Yoshida N., 2004, MNRAS, 350, 893
Hamana T., Oguri M., Shirasaki M., Sato M., 2012, MNRAS, 425, 2287
Hamana T., Sakurai J., Koike M., Miller L., 2015, PASJ, 67, 34
Harnois-Déraps J., Van Waerbeke L., 2015, MNRAS, 450, 2857
Hartlap J., Simon P., Schneider P., 2007, A&A, 464, 399
Henry J. P., 2000, ApJ, 534, 565
Heymans C. et al., 2012, MNRAS, 427, 146
Heymans C. et al., 2013, MNRAS, 432, 2433
Hildebrandt H. et al., 2012, MNRAS, 421, 2355
Hildebrandt H. et al., 2016, MNRAS, 463, 635
Hildebrandt H. et al., 2017, MNRAS, 465, 1454
Hoekstra H., 2001, A&A, 370, 743
Hoekstra H., Hartlap J., Hilbert S., van Uitert E., 2011, MNRAS, 412, 2095
Hoekstra H., Herbonnet R., Muzzin A., Babul A., Mahdavi A., Viola M., Cacciato M., 2015, MNRAS, 449, 685
Jarvis M. et al., 2016, MNRAS, 460, 2245
Jee M. J., Tyson J. A., Hilbert S., Schneider M. D., Schmidt S., Wittman D., 2016, ApJ, 824, 77
Joudaki S. et al., 2017a, MNRAS, 465, 2033
Joudaki S. et al., 2017b, MNRAS, preprint (arXiv:1707.06627)
Kacprzak T. et al., 2016, MNRAS, 463, 3653
Kaiser N., Squires G., 1993, ApJ, 404, 441
Kaiser N., Squires G., Broadhurst T., 1995, ApJ, 449, 460
Kilbinger M., 2015, Rep. Prog. Phys., 78, 086901
Kilbinger M. et al., 2013, MNRAS, 430, 2200
Köhlinger F. et al., 2017, MNRAS, 471, 4412
Kruse G., Schneider P., 1999, MNRAS, 302, 821
Kuijken K. et al., 2015, MNRAS, 454, 3500
Laureijs R. et al., 2011, preprint (arXiv:1110.3193)
Leauthaud A. et al., 2017, MNRAS, 467, 3024
Lewis A., Bridle S., 2002, Phys. Rev. D, 66, 103511
Lin C. A., Kilbinger M., 2015, A&A, 576, 24
Liske J. et al., 2015, MNRAS, 452, 2087
Liu J., Haiman Z., 2016, Phys. Rev. D, 94, 3533
Liu X., Wang Q., Pan C., Fan Z. H., 2014, ApJ, 784, 31
Liu J., Petri A., Haiman Z., Hui L., Kratochvil J. M., May M., 2015a, Phys. Rev. D, 91, 063507
Liu X. et al., 2015b, MNRAS, 450, 2888
Liu X. et al., 2016, Phys. Rev. Lett., 117, 051101
Mandelbaum R., Seljak U., Kauffmann G., Hirata C., Brinkmann J., 2006, MNRAS, 368, 715
Mandelbaum R. et al., 2015, MNRAS, 450, 2963
Mandelbaum R. et al., 2017, PASJ, preprint (arXiv:1705.06745)
Marian L., Smith R. E., Hilbert S., Schneider P., 2012, MNRAS, 423, 1711
Marian L., Smith R. E., Hilbert S., Schneider P., 2013, MNRAS, 432, 1338
Martinet N., Bartlett J. G., Kiessling A., Sartoris B., 2015, A&A, 581, A101
Martinet N. et al., 2017, MNRAS, preprint (arXiv:1709.07678)
Maturi M., Angrick C., Pace F., Bartelmann M., 2010, A&A, 519, 23
Mead A. J., Peacock J. A., Heymans C., Joudaki S., Heavens A. F., 2015, MNRAS, 454, 1958
Miller L. et al., 2013, MNRAS, 429, 2858
Miyatake H. et al., 2015, ApJ, 806, 1
Navarro C., Frenk C., White S. D. M., 1996, ApJ, 462, 563
Navarro C., Frenk C., White S. D. M., 1997, ApJ, 490, 493
Oguri M., Hamana T., 2011, MNRAS, 414, 1851
Osato K., Shirasaki M., Yoshida N., 2015, ApJ, 806, 186
Planck Collaboration XIII, 2016a, A&A, 594, A13
Planck Collaboration XXIV, 2016b, A&A, 594, A24
Radovich M. et al., 2017, A&A, 598, 107
Rozo E. et al., 2010, ApJ, 708, 645
Schneider P., 1996, MNRAS, 283, 837
Seitz C., Schneider P., 1995, A&A, 297, 287
Seitz C., Schneider P., 1997, A&A, 318, 687
Shan H. Y. et al., 2012, ApJ, 748, 56
Shan H. Y. et al., 2014, MNRAS, 442, 2534
Sifón C., Hoekstra H., Cacciato M., Viola M., Köhlinger F., van der Burg R. F. J., Sand D. J., Graham M. L., 2015, A&A, 575, A48
Tang J. Y., Fan Z. H., 2005, ApJ, 635, 60
Troxel M. A. et al., 2017, Phys. Rev. D, preprint (arXiv:1708.01538)
van Uitert E. et al., 2017, MNRAS, preprint (arXiv:1706.05004)
Van Waerbeke L., 2000, MNRAS, 313, 524
Velliscig M., van Daalen M., Schaye J., McCarthy I., Cacciato M., Le Brun A., Dalla Vecchia C., 2014, MNRAS, 442, 2641
Vikhlinin A. et al., 2009, ApJ, 692, 1060
Watson W. A., Iliev I., D'Aloisio A., Knebe A., Shapiro P., Yepes G., 2013, MNRAS, 433, 1230
Yang X., Kratochvil J. M., Wang S., Lim E. A., Haiman Z., May M., 2011, Phys. Rev. D, 84, 043529
Yang X., Kratochvil J. M., Huffenberger K., Haiman Z., May M., 2013, Phys. Rev. D, 87, 023511
Yuan S., Liu X., Pan C., Wang Q., Fan Z. H., 2017, ApJ, submitted
Zuntz J. et al., 2017, MNRAS, preprint (arXiv:1708.01533)

APPENDIX A: COSMOLOGICAL DEPENDENCE OF WL PEAK MODEL

Here we present tests of the Fan et al. (2010) peak model against simulations. From a suite of simulations with 158 different cosmological models from Dietrich & Hartlap (2010), each with a different (Ω_m, σ_8), we choose nine cosmological models (Fig. A1) to

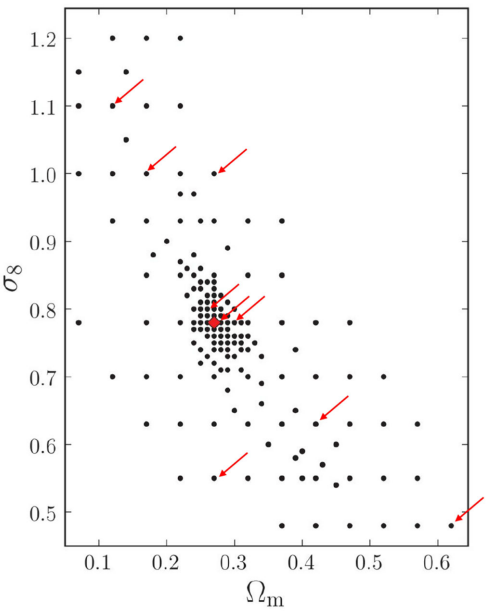

Figure A1. The spatial distribution of 158 different cosmologies in the Ω_m–σ_8 plane. The red diamond marks the fiducial cosmology at (Ω_m, σ_8) = (0.27, 0.78). The red arrows denote the cosmologies used for WL peak model tests.

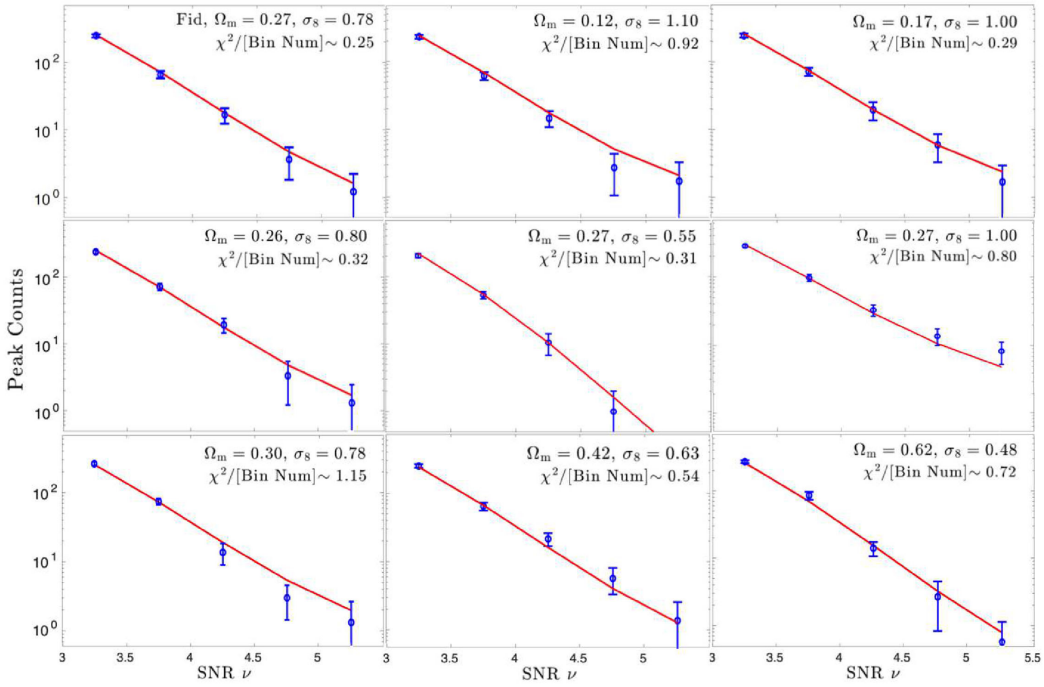

Figure A2. The peak count distribution of the selected simulations. The corresponding solid lines are the theoretical prediction with the input cosmological parameters.

perform our tests. We also include the 'fiducial' $(\Omega_m, \sigma_8) = (0.27, 0.78)$ cosmological model from Dietrich & Hartlap (2010), because of its increased sampling.

Each of these simulations is stored in the form of single galaxy catalogue (containing position, redshift and shear) where galaxies have been sampled uniformly over a 6×6 deg^2 patch with number density $n_g \sim 25$ arcmin^{-2}. From each catalogue, we generate a mock sample by randomly sampling galaxies to reproduce the galaxy number density and redshift distribution of our data set.

For each non-fiducial cosmology, Dietrich & Hartlap (2010) produce a single simulation box with five different (random) LOS, with a total area of $\sim$180 deg^2. We then sample our galaxies three times for each LOS, thus generating three sets of mocks for each model. After excluding boundaries, the final on-sky area for each of our eight non-fiducial cosmologies is $\sim$150 deg^2, each sample three times. For the fiducial cosmology, however, there are 35 individual simulation boxes, each with five different random LOS. For this cosmology, we sample our galaxy only once per LOS, thus generating 35 individual mock catalogues with a final on-sky area of $\sim$1050 deg^2. We therefore end up with 295 individual mock catalogues to analyse, generated from 215 individual LOS across 43 individual simulation boxes with nine different cosmologies.

For each mock catalogue, we perform a mass reconstruction and peak identification, and then fit the peak distribution with the theoretical predictions of Fan et al. (2010). Fig. A2 shows the results of these fits for each of our nine cosmologies. In the figure, the symbols show the peak counts averaged:

(i) over 35 mocks for the fiducial mode, and
(ii) over three mocks for the others.

The uncertainties on the data points are the expected analytic uncertainties in peak counts given a survey area of 150 deg^2. We also present the value of $\chi^2/n_{\rm bins}$ for each model fit in the upper right of each panel.

In all cases, we see that the model predications agree well with the simulation results. Note, however, that the simulation mocks here are somewhat idealized; for instance, there is no masking in these mocks. None the less, they are sophisticated enough for the purpose of testing the peak model performance. In Appendix C, we show analyses of mock images that replicate KiDS more accurately.

APPENDIX B: RESIDUAL NOISE PROPERTIES

One assumption within the peak model of Fan et al. (2010) is that the residual shape noise field is well described by a Gaussian random field. Van Waerbeke (2000) demonstrates that, when the effective number of source galaxies within the smoothing kernel is larger than $\sim$10, the residual shape noise is approximately Gaussian to a good degree. For the KiDS-450 data set used here, $n_{\rm eff} \sim 7.5$ arcmin^{-2}. Therefore, for a smoothing scale $\theta_G = 2$ arcmin, we expect that the Gaussian approximation for the noise field should be valid. However, the source galaxy distribution varies from tile to tile, and within a tile the galaxy distribution is also truly random; there are far fewer source galaxies in regions that are heavily masked. We therefore need to set appropriate selection criteria to ensure the validity of the Gaussian noise approximation that we have assumed.

From the noise maps described in Section 3.3, we analyse the one-point probability distribution function of the noise, and corresponding noise peak distribution, with different n_g and filling factor selection criteria. In Fig. B1, the solid black line shows the shape of the assumed Gaussian peak noise distribution. Blue symbols are the results from noise maps without applying any selection criteria, and clearly show some non-Gaussianity at high SNR. The other symbols and lines represent the results with different selection criteria as shown in the legend. Uncertainties on the data are estimated using a bootstrap analysis. From the figure, we can see that, while

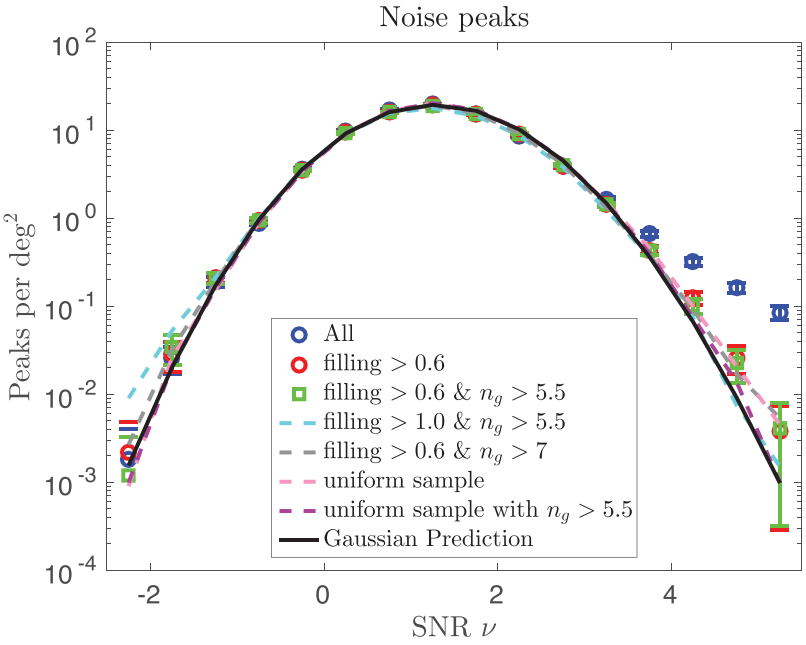

Figure B1. Noise properties for different n_g and filling factors. The solid black line is the corresponding Gaussian prediction for the peak distribution. Blue symbols are the results from noise maps without any selection. The other symbols and lines represent the results with different selection criteria. The error bars are evaluated from a bootstrap analysis.

the Gaussian approximation cannot describe the noise peaks well in the raw-counts case, by applying some modest selection criteria the approximation holds quite well. With a requirement of the filling factor $f > 0.6$, which is designed to exclude the mask effects, the peak distribution is much closer to the Gaussian case. With $n_{\rm eff} > 5.5\,{\rm arcmin}^{-2}$, the results can be improved further. Applying even more stringent cuts, we are able to make the noise distribution converge on the Gaussian case almost perfectly; however, this also causes a significant reduction in the number statistics. Finally, we note that, if the galaxy distribution is a purely random selection of galaxies on sky, the noise peak distribution becomes almost a perfect Gaussian when applying the simple $n_{\rm eff} > 5.5\,{\rm arcmin}^{-2}$ selection. In the realistic case where the galaxy distribution is unlikely to be a perfectly random sampling on sky, the agreement with the assumed Gaussian distribution is acceptable (within uncertainties) when applying our modest selection criteria. Thus, in our analysis, to ensure the validity of the Gaussian approximation while maintaining appropriate number statistics, we invoke two selection criteria on filling factor $f > 0.6$ and effective number density $n_{\rm eff} > 5.5\,{\rm arcmin}^{-2}$.

APPENDIX C: MOCK ANALYSIS

Here we present our validation of the full analysis pipeline using mock KiDS-450 data constructed from our simulations. These mocks are generated from the ray-tracing simulations described in Liu et al. (2015b). Briefly, we run a large suite of *N*-body simulations and pad them together to redshift $z = 3$ for ray-tracing calculations. Cosmological parameters in this simulation are chosen to be ($\Omega_{\rm m}$, Ω_Λ, $\Omega_{\rm b}$, h, σ_8, $n_{\rm s}$) = (0.28, 0.72, 0.046, 0.7, 0.82, 0.96). Each box is only used once, and so no repetitive structures occur; shifts and rotations of boxes are therefore not needed. From the simulations, we generate 96 lensing maps each with an area of $3.5 \times 3.5\,{\rm deg}^2$, for a total area of 1176 deg^2. This allows us to create three independent 449.7 deg^2 KiDS-like mocks.[8] For each mock, we generate catalogues using three different random rotations of galaxy intrinsic ellipticities, to produce three sets of shape noise, thus producing nine sets of mock catalogues to be used in this validation test.

The mock catalogue contains the position, observed ellipticity, weight and redshift of each source therein. Each of these parameters is defined such that the mock is an appropriate representation of KiDS.

(i) The position and the shear measurement weight of each galaxy are taken to be the same as that of the KiDS-450 data, and so we are able to appropriately reproduce the KiDS masking in our mocks.
(ii) Galaxy redshifts within the mock are generated by assigning a random value from the DIR redshift distribution of KiDS-450.
(iii) The observed ellipticity of each galaxy is constructed by combining the reduced shear and the intrinsic ellipticity.
(iv) The galaxy reduced shear g is calculated by interpolating the lensing signals from the grids of the simulated lensing maps to the galaxy position (the interpolation is also done in the redshift dimension).
(v) The intrinsic ellipticity is generated by keeping the amplitude of the observed ellipticity of the galaxy, but with its orientation being randomized.

We then parse these mock catalogues through the same pipeline as we do the observed KiDS data to construct convergence maps, tile by tile, and produce the mock WL peak catalogue. These individual catalogues are then used to derive cosmological constraints, as per KiDS.

In Fig. C1, the left-hand panel shows the peak number distributions from the mock data. The symbols in the figure are coloured according to from which of the three independent simulated maps

[8] These mocks are different from the SLICS mocks used in previous KiDS publications (Harnois-Déraps & Van Waerbeke 2015).

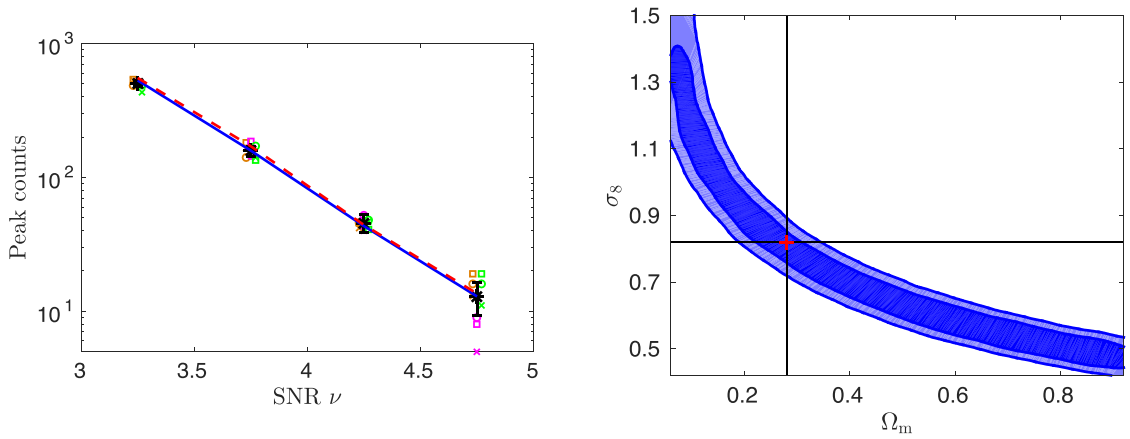

Figure C1. The results of the mock analysis. Left-hand panel: the peak count distribution of the KiDS-450 mock data. The black '*' denotes the average value of the three independent mocks. The error bars are the square root of the diagonal terms of the covariance matrix. The nine sets of symbols with different colours correspond to the three independent mocks with three different noise realizations. The solid blue line is the theoretical prediction with the input cosmological parameters. The dashed red line is the peak count of the smoothed convergence field including a uniform random noise field with the mean noise level of nine mocks. Right-hand panel: cosmological constraints on (Ω_m, σ_8) derived from the KiDS-450 mock peak count. The red '+' denotes the input (Ω_m, σ_8).

they originated. The three symbol types within each colour are the results from different noise realizations. The black '*' denotes the average value per bin from the nine mocks. We estimate the covariance matrix by generating 10^4 bootstrap samples by resampling the 9×454 tiles from the mocks. The error bars associated with each black '*' are derived using the rms of the diagonal elements of the covariance matrix. The solid blue line is the theoretical prediction from Fan et al. (2010), with the input cosmological parameters. The dashed red line is the peak count of the smoothed convergence field from simulation including a uniform random noise field with the noise level of nine mocks, which is in good agreement with the theoretical prediction within 1σ.

The right-hand panel of Fig. C1 shows the derived constraints on (Ω_m, σ_8) using the average peak counts from the mocks. The contours are 1σ and 2σ confidence levels, respectively. The red '+' denotes the input cosmological parameters, which are recovered excellently by the pipeline. We therefore conclude that the pipeline is performing well even when confronted with the complexity of real data.

APPENDIX D: BOOST FACTOR

The cluster member contamination of WL source galaxies depends on the mass and redshift of the cluster. In order to quantify the boost effect that this has on WL peak counts, we therefore should first analyse the mass and redshift distribution of clusters that are responsible for the high-SNR peaks in KiDS-450.

In the noiseless case, a cluster with a given mass and redshift produces a WL peak with a height that can be well predicted given the source redshift distribution (see e.g. Hamana et al. 2004). Fig. D1 shows the fractional contributions of clusters, with different masses and redshifts, to WL peaks of different heights in KiDS. It is seen that, without considering the shape noise, the high-SNR peaks correspond to clusters with masses larger than $3 \times 10^{14}\,\mathrm{M}_\odot$ and in the redshift range up to $z \sim 0.4$.

Taking into account the shape noise, the peak height from a cluster with a given mass and redshift becomes a probability function, whose width is dependent on the noise level. Furthermore, noise peaks can occur in halo regions, further polluting the sample. The effect of the addition of noise to this sample is shown in Fig. D2, whereby the WL peaks become significantly broader in both mass and redshift than that of noiseless case. In the figure, we can see that the contributions to the high-SNR peaks in our analysis are mainly from the massive DM haloes with $M \sim 1$–$5 \times 10^{14}\,h^{-1}\,\mathrm{M}_\odot$ and $z \sim 0.1$–0.6.

While, ideally, we would like to have the precise mass and redshift dependence of cluster member contaminations, this is impractical given the limited number of cluster candidates. Instead, we opt to divide the KiDS cluster candidates (see Radovich et al. 2017) into six bins (see Table D1). We then use these bins to extract the corresponding boost factors, by estimating the excess filling factor (galaxy number overdensity) distribution around cluster candidates. Fig. D3 shows the excess galaxy number density (filling factor) distributions around cluster candidates for each bin.

To analyse how the boost factor affects the WL convergence peaks in halo regions, we build an appropriate set of mocks. For each of the six bins, we pick out a typical halo with the mass and the redshift as indicated in Fig. D4. We model the halo with the NFW profile, and put it in the centre of a $1.2 \times 1.2\,\mathrm{deg}^2$ field. We then distribute source galaxies in the field in two ways:

(1) no boost: we sample galaxies using our standard KiDS n_g and DIR redshift distributions, with random intrinsic ellipticity and reduced shear from the central DM halo;
(2) boost: based on the no boost case, we further resample member galaxies following the excess galaxy number density profile in Fig. D3. Only random intrinsic ellipticities are given to the member galaxies because lensing signals from their own halo should be zero (e.g. Sifón et al. 2015).

Using the same method, we also generate source catalogues with intrinsic ellipticities set to be zero to produce the noiseless cases. Using these galaxy mocks, we then follow the same procedures as done for our KiDS analysis to reconstruct the convergence field. Furthermore, we exclude the outermost ∼0.1 deg regions along each side of the field to suppress the boundary effects. For each halo, we do 1000 realizations according to the positions and intrinsic ellipticity distribution of source galaxies. Finally, as the boost effects can influence both the WL signal and the noise level in halo regions, we consider them separately with the mocks.

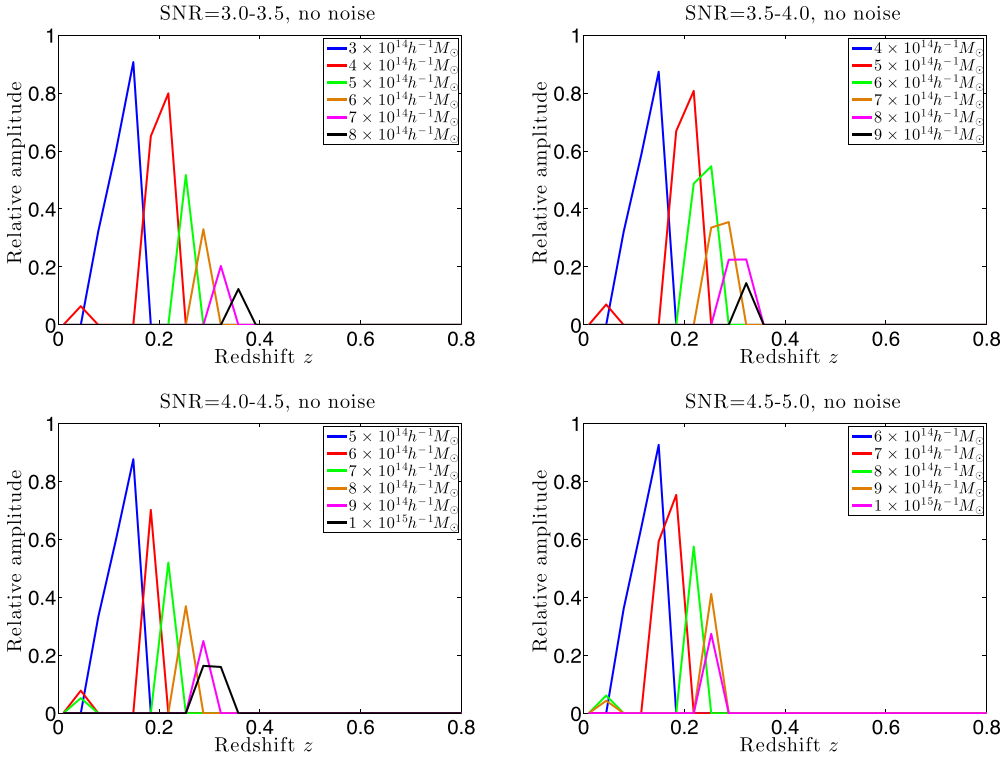

Figure D1. The fractional contributions of clusters with different masses and redshifts to WL peaks of different heights using the KiDS-450 source redshift distribution without the shape noise.

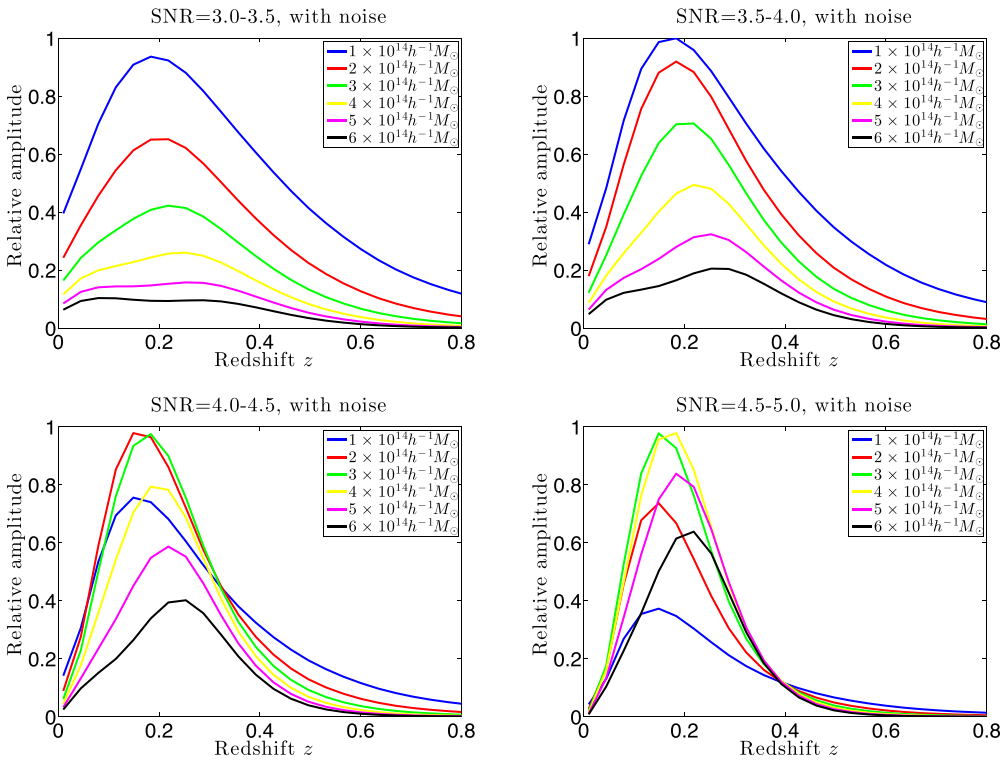

Figure D2. The fractional contributions of clusters with different masses and redshifts to WL peaks of different heights using the KiDS-450 source redshift distribution with KiDS-450-like shape noise.

Table D1. The cluster samples in six mass and redshift bins used in the boost factor measurement.

Bin	Mass range	z_B range	Dilution factor
bin11	$1 \leq M/10^{14}\,\mathrm{M}_\odot\,h^{-1} < 2$	$z_B < 0.35$	1/1.067
bin12	$1 \leq M/10^{14}\,\mathrm{M}_\odot\,h^{-1} < 2$	$z_B \geq 0.35$	1/1.108
bin21	$2 \leq M/10^{14}\,\mathrm{M}_\odot\,h^{-1} < 3$	$z_B < 0.35$	1/1.135
bin22	$2 \leq M/10^{14}\,\mathrm{M}_\odot\,h^{-1} < 3$	$z_B \geq 0.35$	1/1.164
bin31	$3 \leq M/10^{14}\,\mathrm{M}_\odot\,h^{-1} < 4$	$z_B < 0.35$	1/1.259
bin32	$3 \leq M/10^{14}\,\mathrm{M}_\odot\,h^{-1} < 4$	$z_B \geq 0.35$	1/1.254

To estimate the WL peak signal, we estimate the ratio of the convergence value of the central peak between the two cases with and without the boost effects from the 1000 noiseless realizations for each halo. We find the average dilution factors for the six bins (see Table D1). We further test whether a constant boost factor, corresponding to the dilution effects in Table D1, can mimic the real boost effect with radial profiles. We do this by resampling member galaxies according to a constant boost factor, such as 1.067 for the case of bin11. We find that such a constant boost does indeed model the true boost effect on the WL convergence peaks well. Thus, in

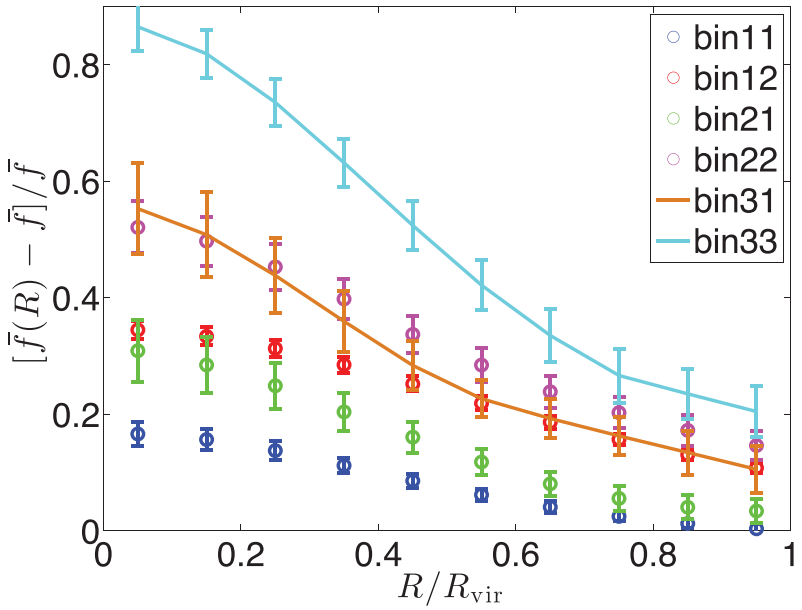

Figure D3. Excess galaxy number density (filling factor) distribution around cluster candidates for each bin. The error bars on the mean are estimated from a bootstrap analysis.

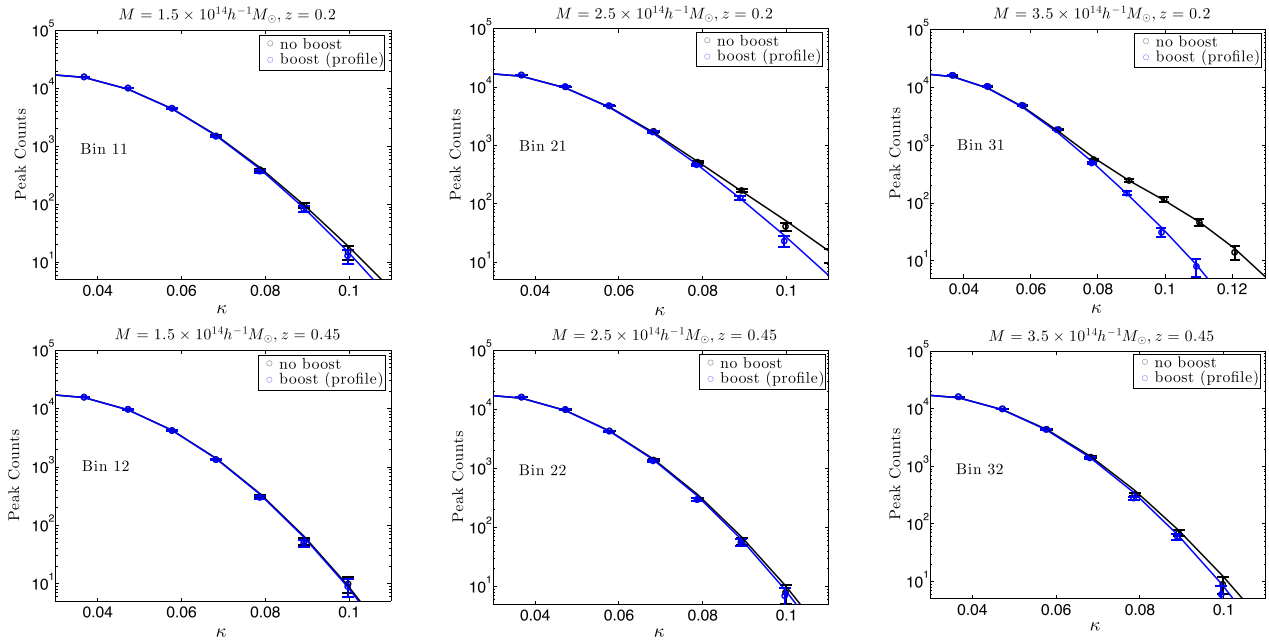

Figure D4. The peak distribution with and without the boost factor effects for different bins. The circles with error bars are the measurement from the mock analysis. The lines with different colours are the corresponding analytical predictions.

the model calculations, we adopt the constant dilution factors in Table D1 in the corresponding six bins.

For the shape noise levels, we consider the halo and field regions individually. We first calculate a global average source number density $n_{\rm g}$ from the data, which includes the excess number density from galaxies in clusters. Compared to this global average, the number density in halo regions $n_{\rm g}^{\rm halo}$ is higher depending on the boost factor shown in Fig. D3, and thus the noise level $\sigma_0^{\rm halo}$ in the halo regions is lower. Correspondingly, the number density in field regions $n_{\rm g}^{\rm field}$ is lower than $n_{\rm g}$, and $\sigma_0^{\rm field}$ is higher than σ_0. The three number densities are related by

$$n_{\rm g} S_{\rm eff} = \sum n_{\rm g}^{\rm halo} S_{\rm eff}^{\rm halo} + n_{\rm g}^{\rm field} S_{\rm eff}^{\rm field}, \tag{D1}$$

where $S_{\rm eff}$, $S_{\rm eff}^{\rm halo}$ and $S_{\rm eff}^{\rm field}$ are the total effective area, the area occupied by haloes and the left-over field area with $S_{\rm eff}^{\rm field} = S_{\rm eff} - \sum S_{\rm eff}^{\rm halo}$, respectively. From $n_{\rm g}^{\rm field}$, we can calculate the noise level $\sigma_0^{\rm field}$. It is noted that $\sum S_{\rm eff}^{\rm halo}$, and thus also $S_{\rm eff}^{\rm field}$, are cosmological model dependent.

Using the above equations, we are able to modify our model calculations to include the boost effect as follows.

(i) Using equation (4) to calculate peaks in halo regions, we divide the halo mass and redshift into the six bins described above. In each bin, we include the corresponding constant dilution factor, which acts to modify the convergence field from the halo. We also modify the noise level according to the average number density of source galaxies in the halo regions.

(ii) Using equation (7) to calculate peaks in field regions, we modify the noise level according to equation (D1).

These modifications are adopted in our fiducial analysis presented in Section 5 including the boost effects.

To test the model performance, Fig. D4 shows the peak counts from our 1000 mock realizations in each of the six bins. The blue and black symbols are the peak counts for the cases with and without the boost effects, respectively. The corresponding solid lines are our model predictions, which demonstrate a good agreement with the data in both cases.

This paper has been typeset from a TEX/LATEX file prepared by the author.